Flow Turbulence Combust (2013) 91:281–317
DOI 10.1007/s10494-013-9462-z

On the Application of the Levenberg–Marquardt Method in Conjunction with an Explicit Runge–Kutta and an Implicit Rosenbrock Method to Assess Burning Velocities from Confined Deflagrations

A. E. Dahoe · T. Skjold · D. J. E. M. Roekaerts · H. J. Pasman · R. K. Eckhoff · K. Hanjalic · M. Donze

Received: 25 November 2011 / Accepted: 22 April 2013 / Published online: 10 May 2013

Abstract The potential of the Levenberg–Marquardt method combined with an explicit Runge–Kutta method for non-stiff systems, and, an implicit Rosenbrock method for stiff systems to investigate burning velocities using explosion bombs was

A. E. Dahoe (✉)
Faculty of Art, Design and the Built Environment, University of Ulster, Northern Ireland, UK
e-mail: arief.dahoe@gmail.com

T. Skjold
Department of Physics and Technology, University of Bergen & GexCon AS, Bergen, Norway
e-mail: trygve@gexcon.com

D. J. E. M. Roekaerts
Section Fluid Mechanics, Department Process and Energy, Delft University of Technology, Delft, The Netherlands
e-mail: d.j.e.m.roekaerts@tudelft.nl

H. J. Pasman
Mary Kay O'Connor Process Safety Center, Texas A&M University, College Station, TX, USA
e-mail: hjpasman@gmail.com

R. K. Eckhoff
Department of Physics and Technology, University of Bergen, Bergen, Norway
e-mail: Rolf.Eckhoff@ift.uib.no

K. Hanjalic
Chemical Engineering Department, Delft University of Technology, Delft, The Netherlands
e-mail: khanjalic@gmail.com

K. Hanjalic
Novosibirsk State University, Novosibirsk, Russia

M. Donze
Faculty Civil Engineering and Geosciences, Delft University of Technology, Delft, The Netherlands
e-mail: m.donze@xs4all.nl

explored. The implementation of this combination of methods was verified on three benchmark test problems, and, by the application of two integral balance models to laminar hydrogen-air and methane-air explosions. The methodology described here was subsequently applied to quantify the coefficients of a turbulent burning velocity correlation for a methane-air explosion in the decaying flow field of the standard 20-litre explosion sphere. The outcome of this research indicates that the usefulness of the 20-litre sphere can be extended beyond the measurement of practical explosion parameters. When combined with the methodology in this paper, turbulent burning velocity correlations can be assessed in different parts of the Borghi-diagram.

Keywords Deflagration · Burning velocity · Flame thickness · Least-squares minimisation · Stiff integration

1 Introduction

Knowledge of the laminar and turbulent burning velocity has become a prerequisite for the assessment of explosion hazards [1–8]. Various experimental methods exist for the determination of the burning velocity [9, 10]. These are the Bunsen flame method, the flat flame method, the stagnation flame method, and the outwardly propagating flame method. The latter include the constant volume bomb method (centrally ignited flame, double kernel method) and the constant pressure bomb method (soap bubble method, dual chamber method [11]). The present paper concentrates on using the constant volume bomb method. In this method a combustible mixture is ignited to deflagrate from the centre of an explosion vessel outwards. Two approaches exist to determine the burning velocity from such experiments [9, 10]: methods that rely on a combination of direct imaging of the flame trajectory and measuring the pressure-time history, and, methods relying on the pressure-time history alone. Expressions for the determination of the burning velocity from optical cinematography of the flame radius combined with pressure-time recordings are given in [10, p. 443]. Methods that extract the laminar burning velocity from pressure-time recordings only are given in [9, p. 271]. The method described here belongs in the latter category, whereby the burning velocity is determined by least-squares fitting a differential equation for the pressure development via its numerical solution to experimental pressure time-curves.

This paper is organised as follows. Section 2 describes the application of the Levenberg–Marquardt method in conjunction with a Runge–Kutta and a Rosenbrock method to three benchmark test problems. A particular problem encountered with the explosion models in this work, and integral balance models in general, is the occurrence of stiffness. Least-squares fitting differential equations requires the model to be augmented with additional differential equations (Appendix C). But this may result in a stiff system, even when the original model is non-stiff. When this happens it becomes necessary to resort to so called ‘stiff integration methods’. The Rosenbrock method [12, 13] is considered to be appropriate for stiff systems. Combining the Levenberg–Marquardt method with numerical integration methods for differential equations is not straightforward and prone to error. Therefore it is the purpose of this section to provide a verification of the implementation of this combination of methods.

Section 3 describes the explosion models applied in this work: a thin-flame deflagration model (Eqs. 32 and 33) where the conversion of reactants into combustion products occurs in a flame zone of zero thickness, and, a three-zone deflagration model (Eqs. 34–39 and 34–43) with a non-zero flame thickness. The models are equipped with correlations (Eqs. 32, 38 and 39) for the effect of pressure and temperature on the laminar burning velocity and laminar flame thickness. For turbulent deflagrations, Eqs. 40 and 41 are implemented for the transient behaviour of the turbulent burning velocity and turbulent flame thickness. While more advanced integral balance models exist in the literature (e.g. [14]), the thin-flame and three-zone deflagration models were selected because they are easier to implement into the numerical methods described in Appendices A, B and C.

Section 4 presents an analysis of turbulent burning velocity and turbulent flame thickness correlations. The availability of a satisfactory turbulent flame propagation model is of crucial importance for the analysis of pressure-time traces of a turbulent explosion. Difficulties with the assessment of such correlations already begin with forming an accurate picture of what might constitute a turbulent flow [15–17], even for an inert fluid without combustion. Then there is also the question of which turbulence features to apply. Turbulent flames have properties such as an overall propagation rate of the flame brush and its thickness. The consequential energy release is determined on a micro-scale by a local burning velocity and the total flame surface area of flamelets. All this depends on an interplay between turbulence, thermodynamics, chemical kinetics, diffusion rates of components and heat effects. Because a detailed description due to the dynamics involved is not feasible, the overall effect is expressed by a turbulent burning velocity.

When a turbulent flow field is characterised by its turbulence intensity, v_{rms}, experimental data appear to correlate according to a relationship of the form $S_{uT}/S_{uL} = f(v_{\mathrm{rms}}/S_{uL})$. Similarly, when the turbulence intensity, v_{rms}, and the turbulence macro length scale, ℓ_t, are used then experimental data are seen to correlate as $S_{uT}/S_{uL} = f(v_{\mathrm{rms}}/S_{uL}, \ell_t/\delta_L)$. Tuning of model coefficients is required to establish agreement between predictions and experimental observations. To assess the appropriateness of existing correlations, several quantitative models proposed over the period 1940–2012 are collected (Table 1) and compared with experimental data (Fig. 5). While these correlations are supported by experimental data, and/or, rigorous theoretical derivation, their form suggests that they are specific instances of more general ones, yet to be discovered. However, no such universal expressions have been derived from 'first principles' [18]. Due to the absence of a satisfactory correlation for the turbulence conditions in this work, dimensional analysis is applied to obtain a set of expressions for the turbulent burning velocity and the turbulent flame thickness, Eqs. 40 and 41. Their coefficients are estimated by curve-fitting them to experimental burning velocity data (Fig. 7).

Section 5 describes the determination of the laminar burning velocity from the pressure-time traces of confined deflagrations. The integral balance models of Section 3 are least-squares fitted to the pressure-time trace of an initially quiescent stoichiometric hydrogen-air and methane-air mixture. The resulting laminar burning velocities are compared with literature data to verify the implementation of the models into the numerical methods. Next, the possibility to determine the laminar burning velocity from turbulent deflagrations, and, the assessment of turbulent burning velocity correlations, are explored by analysing the pressure-time curve of a turbulent methane-air explosion in a decaying flow field. A final section summarises the findings and conclusions arising from this work.

Table 1 A compilation of turbulent burning velocity models for premixed flame propagation in chronological order of appearance

Model	Reference
(1) $\frac{S_{uT}}{S_{uL}} = 1 + \frac{v'_{\mathrm{rms}}}{S_{uL}}$	[42, 43]
Note: Analysis of instantaneous laminar flame area within a turbulent flame brush. Instantaneous laminar flame area is assumed to increase linearly with v'_{rms}.	
(2) $\frac{S_{uT}}{S_{uL}} = \sqrt{1 + \left(\frac{v'_{\mathrm{rms}}}{S_{uL}}\right)^2}$	[44, 45]
Note: Analysis of instantaneous laminar flame area within a turbulent flame brush. Distorted laminar flame is assumed to consist of conical bulges. Effect of turbulence taken into account by surface area ratio between cone mantle and cone base.	
(3) $\frac{S_{uT}}{S_{uL}} = 1 + \frac{v'_{\mathrm{rms}}}{S_{uL}}$ Same as (1).	[46]
(4) $\frac{S_{uT}}{S_{uL}} = 1 + \sqrt{\frac{5}{12}}\frac{v'_{\mathrm{rms}}}{S_{uL}}$ (5) $\frac{S_{uT}}{S_{uL}} = 1 + \sqrt{2}\left(\frac{v'_{\mathrm{rms}}}{S_{uL}}\right)^{\frac{1}{2}}$	
Note: Time-scale analysis of r.m.s. displacement [47] within interaction time between flame element and turbulent eddy. Equation 3: weak turbulence ($\ell_t/v'_{\mathrm{rms}} \gg \delta_l/S_{uL}$) Eq. 4: intermediate turbulence ($\ell_t/v'_{\mathrm{rms}} \approx \delta_l/S_{uL}$). Equation 5: strong turbulence ($\ell_t/v'_{\mathrm{rms}} \ll \delta_l/S_{uL}$).	
(6) $\frac{S_{uT}}{S_{uL}} = \sqrt{1 + \left(\frac{2v'_{\mathrm{rms}}}{S_{uL}}\right)^2}$	[48]
Note: Analysis of intersection between eddies and laminar flame. Eddies assumed to have diameter ℓ_t and a sinusoidal velocity profile characterised by v'_{rms} [36].	
(7) $\frac{S_{uT}}{S_{uL}} = 1 + C\left(\frac{v'_{\mathrm{rms}}}{S_{uL}}\right)^2$	[49]
Note: Analysis interaction of laminar flame with isotropic turbulence [36, 49].	
(8) $\frac{S_{uT}}{S_{uL}} = 1 + \left(\frac{v'_{\mathrm{rms}}}{S_{uL}}\right)^2$	[50]
Note: Analysis of the longitudinal displacement of the reactive-diffusive zone by turbulence in an Eulerian frame of reference.	
(9) $\frac{S_{uT}}{S_{uL}} = \left\{\frac{1}{2}\left[1 + \left[1 + C\left(\frac{v'_{\mathrm{rms}}}{S_{uL}}\right)^2\right]^{\frac{1}{2}}\right]\right\}^{\frac{1}{2}}$	[51]
Note: An extension of model (8) with thermal expansion taken into account [37].	
(10) $\frac{S_{uT}}{S_{uL}} = C\left(\frac{v'_{\mathrm{rms}}}{S_{uL}}\right)^n$ $C = 3.5, n = 0.7$	[52]
Note: Analysis of flame-turbulence interaction. Turbulence characterised by single velocity scale and single length scale [37].	
(11) $\frac{S_{uT}}{S_{uL}} = f(K)$ where $K = C\mathrm{Re}_{\ell_t}^{-\frac{1}{2}}\left(\frac{v'_{\mathrm{rms}}}{S_{uL}}\right)^2$	[53]
Note: $C = 0.157$. Two-eddy theory. Rate of burning equal to product of rate of eddy decay and amount of mixture that reacts chemically during eddy lifetime. Localized reaction rate within an eddy is expressed by laminar burning velocity [53]. K is the Karlovitz stretch factor [34].	
(12) $\frac{S_{uT}}{S_{uL}} = C\left(\frac{v'_{\mathrm{rms}}}{S_{uL}}\right)$ $C = 2.1$	[54]
Note: Monte Carlo solution of a modelled transport equation for the joint probability density function (pdf) of velocity and reaction progress variable [54].	
(13) $\frac{S_{uT}}{S_{uL}} = \mathrm{Re}_{\ell_K}^{\frac{3}{2}}\left(\frac{v'_{\mathrm{rms}}}{S_{uL}}\right)^{\frac{1}{2}}$	[55]
Note: Analysis of exchanges of state (burned or unburned) between adjacent fluid elements along a discretized line element in the streamwise direction [55].	

Table 1 (continued)

Model	Reference
(14) $\frac{S_{uT}}{S_{uL}} = \left\{\beta\left[1-\left(1-\beta^{-1}\right)\exp\left(-\alpha\frac{v'_{\mathrm{rms}}}{S_{uL}}\right)\right]\right\}^{D-2}$	[56]
Note: Fractal modelling of laminar flame surface with fractal dimension $D = 2.32$–2.40 [56–59], outer cutoff $\ell_o = \ell_t$, and inner cutoff $\ell_i = \ell_K$. $\mathrm{Re}_{\ell_t} = \rho v'_{\mathrm{rms}}\ell_t/\mu$, $\alpha = (A_t/\mathrm{Re}_{\ell_t})^{1/4}$ and $\beta = (A_t/\mathrm{Re}^3_{\ell_t})^{1/4}$. $A_t = 0.37$ from turbulent pipe flow data [53, 56, 60].	
(15) $\frac{S_{uT}}{S_{uL}} = \frac{v'_{\mathrm{rms}}}{S_{uL}}$	[61]
Note: Fractal modelling of laminar flame surface in turbulent flow. Flame surface: outer cutoff $\ell_o = \ell_t$ and inner cutoff equal to Gibson length scale, $\ell_i = \ell_G$. [62].	
(16) $\frac{S_{uT}}{S_{uL}} = \exp\left[v'^2_{\mathrm{rms}}/S_{uT}^2\right]$	[18, 63]
Note: Analysis of very thin reaction zone in a turbulent flow field [18]. Flame represented by scalar field $G(\boldsymbol{x}, t)$ which propagates according to [64, 65] $\partial G/\partial t + \boldsymbol{v}\cdot\nabla G = S_{uL}\lvert\nabla G\rvert$. Reference [18] derives (16) by dynamic re-normalisation group analysis to G-equation. Reference [63] derives (16) from two distinct expressions for turbulent flame brush thickness while assuming exponential growth of interface between parcels of reactants and products.	
(17) $\frac{S_{uT}}{S_{uL}} = 1 + C\left(v'_{\mathrm{rms}}/S_{uL}^{1/2}\right)$ $\quad C = 5.3$	[66]
Note: Curve fit to experimental burner data (turbulence by perforated plate) [66].	
(18) $\frac{S_{uT}}{S_{uL}} = 1 + C\mathrm{Re}_{\ell_t}^{\frac{1}{4}}\left(\frac{v'_{\mathrm{rms}}}{S_{uL}}\right)^{\frac{1}{2}} = 1 + C\mathrm{Re}_{\delta_L}^{\frac{1}{4}}\mathrm{Da}^{\frac{1}{4}}\left(\frac{v'_{\mathrm{rms}}}{S_{uL}}\right)^{\frac{3}{4}}$	[37]
Note: $C = \sqrt[4]{2/15} \approx 0.6$. Application of two distinct expressions for the turbulent flame brush thickness in conjunction with an estimate of the mean distance the flame must travel to consume the mixture between dissipative vortex tubes and the relationship $\lambda_T/\ell_t = \sqrt{15}\mathrm{Re}_{\ell_t}^{-1/2}$ [15, 16]. The Taylor microscale, λ_T, is the spacing between the vortex tubes. Curve-fitting to more than 200 data points for 15 mixtures reported by eight different research groups gave a value of $C = 0.62$ [37].	
(19) $\frac{S_{uT}}{S_{uL}} = 1 + S_{uL}^{1/4}\left(\frac{v'_{\mathrm{rms}}}{S_{uL}}\right) = 1 + \left(\frac{\delta_L v_{\mathrm{rms}}}{\ell_t}\right)^{\frac{1}{4}}\mathrm{Da}^{\frac{1}{4}}\left(\frac{v'_{\mathrm{rms}}}{S_{uL}}\right)$	[67]
Note: Curve fit to experimental turbulent burning velocities of methane-air, hydrogen-air and methane-hydrogen-air mixtures in fan-stirred vessels (651 spherical bomb and $1\,\mathrm{m}^3$ cylindrical vessel).	
(20) $\frac{S_{uT}}{S_{uL}} = C\mathrm{Le}^{-0.3}\mathrm{Re}_{\ell_t}^{0.15}\left(\frac{v'_{\mathrm{rms}}}{S_{uL}}\right)^{0.4}$ $\quad C = 1.534$	[34]
Note: Curve fit to 1650 experimental data points by 20 different groups [34, 68].	
(21) $\frac{S_{uT}}{S_{uL}} = 1 + C\mathrm{Da}^{\frac{1}{4}}\left(\frac{v'_{\mathrm{rms}}}{S_{uL}}\right)$ $\quad C = 0.51$	[69]
Note: Analysis of flame front motion from solution of Favre-averaged governing equations in spherical coordinates with Bray-Moss-Libby formalism as closure model [70–72] and a model for local combustion failure [69].	
(22) $\frac{S_{uT}}{S_{uL}} = 1 + \left(\frac{v'_{\mathrm{rms}}}{S_{uL}}\right)^{1/2} = 1 + \left(\frac{\ell_t}{\delta_L}\right)^{\frac{1}{4}}\mathrm{Da}^{\frac{1}{4}}\left(\frac{v'_{\mathrm{rms}}}{S_{uL}}\right)^{\frac{3}{4}}$	[73]
Note: Experimental analysis of a downward propagating premixed methane-air flame through a nearly isotropic turbulent flow field in a tube [73].	
(23) $\frac{S_{uT}}{S_{uL}} = 1 + C\left(\frac{\ell_t}{\delta_L}\right)^{1/4}\left(\frac{v'_{\mathrm{rms}}}{S_{uL}}\right)^{3/4} = 1 + C\mathrm{Da}^{\frac{1}{4}}\left(\frac{v'_{\mathrm{rms}}}{S_{uL}}\right)$	[74]
Note: $C = \sqrt[4]{2/15} \approx 0.6$. Application of a model originating from Refs. [37, 75] to upward propagating potato starch dust-air flames in a tube [74, 76].	
(40) $\frac{S_{uT}}{S_{uL}} = 1 + C'\mathrm{Da}^{a'}\left(\frac{v'_{\mathrm{rms}}}{S_{uL}}\right)^{b'}$	[This work]
Note: Dimensional analysis. Simplification of equation (46).	

A comparison with experimental turbulent burning velocities is given in Fig. 5

2 Application of the Levenberg–Marquardt Method in Conjunction with an Explicit Runge–Kutta and an Implicit Rosenbrock Method to Three Benchmark Test Problems

This section describes the application of the Levenberg–Marquardt method in conjunction with a Runge–Kutta and the Rosenbrock method to three benchmark test problems. The individual methods, and the methodology to combine them in order to cope with systems of differential equations are given in Appendices A, B and C. The purpose of this section is solely to verify their implementation (Algorithm 1 in Appendix C) and assess the computational cost when stiffness occurs.

The first benchmark problem is taken from [19]. It consists of a system of two autonomous ordinary differential equations,

$$\frac{dy_0}{dx} = (2a_0 - a_1)y_0 + (2a_0 - 2a_1)y_1 \qquad y_0(0) = 1 \tag{24}$$

$$\frac{dy_1}{dx} = (-a_0 + a_1)y_0 + (-a_0 + 2a_1)y_1 \qquad y_1(0) = 0 \tag{25}$$

which can be solved analytically. The solution is

$$y_0(x) = 2e^{a_0 x} - e^{a_1 x} \tag{26}$$

$$y_1(x) = -e^{a_0 x} + e^{a_1 x} \tag{27}$$

A synthetic data-set (Fig. 1) containing random data was generated using Eqs. 26 and 27. The spread in y_0 and y_1 was introduced by generating random deviates with a Gaussian distribution in the parameters a_0 and a_1:

$$P(a_k)da_k = \frac{1}{\sigma_{a_k}\sqrt{2\pi}} \exp\left[-\frac{(a_k - \mu_{a_k})^2}{2\sigma_{a_k}^2}\right] da_k. \tag{28}$$

The parameters were assigned values of $a_0 = -1$ and $a_1 = -1000$. A total of 15,000 realisations were computed by the Box–Muller transform [20–23] at 30 discrete instances x^k, each containing 500 realisations of y_0 and y_1. Thus, at each location x^k:

$$\mu^k_{y_j}(x^i) = \frac{1}{M}\sum_{i=0}^{M-1} y^i_j(x^k) \quad \text{and} \quad \sigma^k_{y_j}(x^k) = \sqrt{\frac{1}{M}\sum_{i=0}^{M-1}\left[y^i_j(x^k) - \mu_{y_j}(x^k)\right]^2} \tag{29}$$

where $M = 500$ and $0 \leq k < M$. Each histogram in Fig. 1 depicts the frequency distribution of 15,000 realisations and a comparison with the probability distribution (solid curve) given by Eq. 28. The classical and extended Levenberg–Marquardt method were subsequently applied to fit algebraic Eqn. 26 and 27, and, differential Eqs. 24 and 25 to the synthetic data-set. The iteration-tableaus in Appendix D indicate that the extended method is capable of recovering the parameters a_k and the standard errors ϵ_{a_k} to the same extent as the classical method. The iteration-tableaus show that the values of a_k, da_k, and $\chi^2(\boldsymbol{a})$ are almost identical. The application of the perturbation (89)–(91) instead of the analytical solution to determine the additional initial conditions of system (84) does not distort the iteration sequence. It must be noted, however, that despite being more advanced, the Rosenbrock method needs about 15 % more integration steps than the Runge–Kutta method to cope with

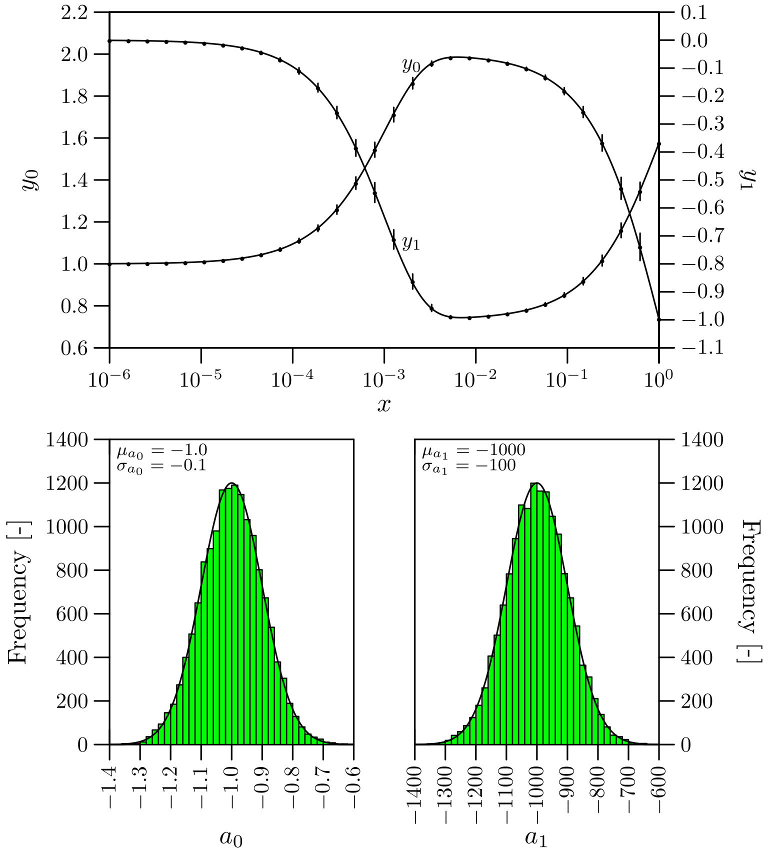

Fig. 1 Synthetic data-set for y_0 and y_1 according to systems (24) and (25) with random values of a_0 and a_1. The frequency distributions of a_0 and a_1 are shown in the *lower part*. Each data point indicated by solid markers in the *upper-part* is the mean value of 500 realisations. The *error-bars* are twice the standard deviation. The *solid curves* represent y_0 and y_1 resulting from Eqs. 26 and 27 with $a_0 = -0.1$ and $a_1 = -1000$. The frequency distributions of a_0 and a_1 have mean values $\mu_{a_0} = -1.0$ and $\mu_{a_1} = -1000$, and, standard deviations $\sigma_{a_0} = -0.1$ and $\sigma_{a_1} = -100$

system (24)–(26). This happens because, in the absence of a stability challenge by stiffness, the Runge–Kutta method benefits from its higher accuracy (5th-order) in comparison with that of the Rosenbrock method (4th-order).

A more challenging benchmark problem is one describing a chemical kinetics model [23–25]:

$$\begin{aligned}
\frac{\partial y_0}{\partial x} &= -a_0 y_0 - a_1 y_0 y_2 & y_0(0) &= 1 \\
\frac{\partial y_1}{\partial x} &= -a_2 y_1 y_2 & y_1(0) &= 1 \\
\frac{\partial y_2}{\partial x} &= -a_0 y_0 - a_1 y_0 y_2 - a_2 y_1 y_2 & y_2(0) &= 0 \qquad (30)
\end{aligned}$$

with $a_0 = 0.013$, $a_1 = 1000$, $a_2 = 2500$

Figure 2 shows the iteration-tableau of the extended Levenberg–Marquardt method with the Rosenbrock method, and, the model-data match between system (30) and a synthetic data-set. Obviously, this problem challenges the stability of the Runge–Kutta method. Computing the solution for $\{a_0 = 0.013, a_1 = 1000, a_2 = 2500\}$ required 131,948 integration steps and 791,688 derivative evaluations. The Rosenbrock method needs only 82 steps and 328 derivative evaluations. A synthetic data-set $(\boldsymbol{x}^i, \hat{\boldsymbol{y}}^i_j, \hat{\boldsymbol{\sigma}}^i_j)$ consisting of 80 realisations with $\hat{\boldsymbol{\sigma}}^i_j = 0.03 \times \hat{\boldsymbol{y}}^i_j$ was generated with $\{a_0 = 0.013, a_1 = 1000, a_2 = 2500\}$. The iteration-tableau demonstrates the ability of the extended method to resolve these parameters when applied with an initial guess $\{a_0 = 0.008, a_1 = 900, a_2 = 2200\}$.

An even more challenging problem concerns a catalytic fluid bed [24, 26, 27]:

$$\begin{aligned}
\frac{\partial y_0}{\partial x} &= b_1(y_2 - y_0) + b_2 y_1 \exp[b_0 - a_0/y_0] && y_0(0) = 761 \\
\frac{\partial y_1}{\partial x} &= a_1[y_3 - y1\{1 + \exp[b_0 - a_0/y_0]\}] && y_1(0) = 0 \\
\frac{\partial y_2}{\partial x} &= b_3 - b_4 y_2 - b_5 y_0 && y_2(0) = 600 \\
\frac{\partial y_3}{\partial x} &= b_6 + b_7 y_1 - b_8 y_3 && y_3(0) = 0.1
\end{aligned} \tag{31}$$

Extended Levenberg-Marquardt method with Rosenbrock method. Analytical Jacobian.												integr.	deriv.	Jacbn.
iter.	λ	a_0	da_0	ϵ_{a_0}	a_1	da_1	ϵ_{a_1}	a_2	da_2	ϵ_{a_2}	$\tilde{\chi}^2(\boldsymbol{a})$	steps	eval.	eval.
init. guess		a_0=8.000·10^{-3}			a_1=9.000·10^{2}			a_2=2.200·10^{3}			9.414·10^{3}	250	1000	250
0	10^{-3}	1.277·10^{-2}	4.772·10^{-3}		9.367·10^{2}	3.667·10^{1}		2.487·10^{3}	4.889·10^{2}		2.226·10^{2}	537	2108	537
1	10^{-4}	1.300·10^{-2}	2.263·10^{-4}		1.006·10^{3}	6.952·10^{1}		2.501·10^{3}	-2.022·10^{2}		5.848·10^{-1}	527	2168	527
2	10^{-5}	1.300·10^{-2}	1.407·10^{-6}		9.994·10^{2}	-6.827·10^{0}		2.501·10^{3}	1.395·10^{1}		1.935·10^{-3}	542	2176	542
3	10^{-6}	1.300·10^{-2}	-2.870·10^{-8}		9.992·10^{2}	-1.393·10^{-1}		2.501·10^{3}	1.404·10^{-1}		1.889·10^{-3}	544	2116	544
4	10^{-7}	1.300·10^{-2}	7.605·10^{-9}		9.992·10^{2}	8.909·10^{-3}		2.501·10^{3}	-7.041·10^{-3}		1.866·10^{-3}	529	2504	529
5	10^{-8}	1.300·10^{-2}	-6.417·10^{-9}		9.992·10^{2}	-1.335·10^{-2}		2.501·10^{3}	1.103·10^{-2}		1.911·10^{-3}	626	2444	626
6	10^{-7}	1.300·10^{-2}	8.700·10^{-9}		9.992·10^{2}	4.484·10^{-3}		2.501·10^{3}	-2.140·10^{-3}		1.974·10^{-3}	611	2504	611
7	10^{-6}	1.300·10^{-2}	2.997·10^{-10}		9.993·10^{2}	4.882·10^{-2}		2.501·10^{3}	-4.525·10^{-2}		1.905·10^{-3}	626	2444	626
8	10^{-7}	1.300·10^{-2}	8.449·10^{-11}		9.992·10^{2}	-4.990·10^{-2}		2.501·10^{3}	4.625·10^{-2}		1.862·10^{-3}	609	2504	609
final:	0.0	1.300·10^{-2}	-1.336·10^{-9}	1.023·10^{-4}	9.993·10^{2}	4.397·10^{-2}	3.861·10^{1}	2.501·10^{3}	-4.148·10^{-2}	2.259·10^{1}	1.952·10^{-3}	593	2436	593

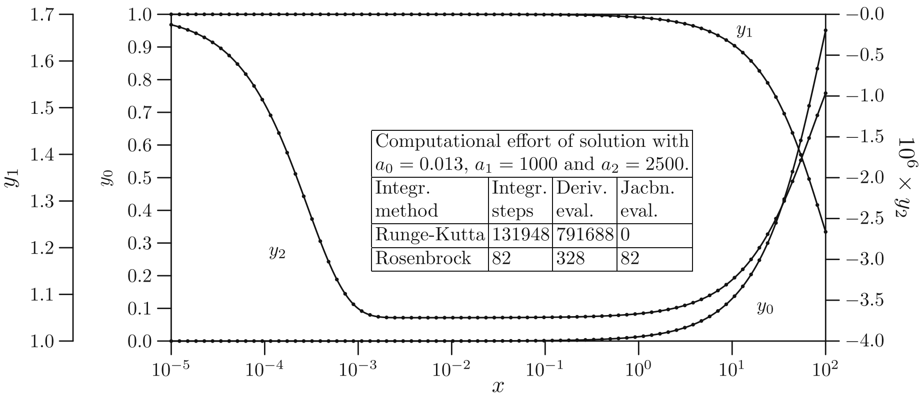

Fig. 2 Iteration-tableau of the extended Levenberg–Marquardt method with the Rosenbrock method when applied to fit system (30) to a synthetic data-set. Initial conditions from perturbation (89)–(91). Prerequisites (Algorithm 1): `maxits` $= 9$, $\tilde{\chi}^2_{\text{crit}} = 10^{-9}$, $\lambda = 10^{-3}$, $h_{\text{init}} = 10^{-4}$, $\epsilon^{\text{rel}} = 10^{-3}$, and $\epsilon^{\text{abs}}_j = 10^{-12}$

with

$$a_0 = 1500, a_1 = 1880, b_0 = 20.7, b_1 = 1.3, b_2 = 10400, b_3 = 1752$$

$$b_4 = 269, b_5 = 267, b_6 = 0.1, b_7 = 320, b_8 = 321$$

A synthetic data-set $(\boldsymbol{x}^i, \hat{\boldsymbol{y}}^i_j, \hat{\boldsymbol{\sigma}}^i_j)$ consisting of 250 realisations with $\{\hat{\boldsymbol{\sigma}}^i_0 = 10.0, \hat{\boldsymbol{\sigma}}^i_1 = 0.001, \hat{\boldsymbol{\sigma}}^i_2 = 10.0, \hat{\boldsymbol{\sigma}}^i_3 = 0.001\}$ was generated with $\{a_0 = 1500, a_1 = 1880\}$. The iteration-tableau in Fig. 3 shows that these parameters can be recovered with an initial guess $\{a_0 = 1600, a_1 = 2000\}$. The middle part of this figure shows how the stability of the Runge–Kutta method is challenged by system (31). The solution by the Runge–Kutta method requires 1,000,002 steps and 6,000,012 derivative evaluations to cover only a part of the integration domain ($10^{-15} \leq x \leq 10^{-4}$) until the

Extended Levenberg-Marquardt method with Rosenbrock method. Numerical Jacobian.									integr.	deriv.	Jacbn.
iter.	λ	a_0	da_0	ϵ_{a_0}	a_1	da_1	ϵ_{a_1}	$\tilde{\chi}^2(\boldsymbol{a})$	steps.	eval.	eval.
init. guess		$a_0=1.600\cdot10^3$			$a_1=2.000\cdot10^3$			$3.088\cdot10^1$	645	2580	645
0	10^{-3}	$1.496\cdot10^3$	$-1.040\cdot10^2$		$1.866\cdot10^3$	$-1.340\cdot10^2$		$9.039\cdot10^{-2}$	1262	5048	1262
1	10^{-4}	$1.500\cdot10^3$	$4.029\cdot10^0$		$1.880\cdot10^3$	$1.385\cdot10^1$		$8.280\cdot10^{-6}$	1127	4508	1127
2	10^{-5}	$1.500\cdot10^3$	$-4.907\cdot10^{-2}$		$1.880\cdot10^3$	$1.129\cdot10^{-1}$		$5.119\cdot10^{-6}$	1140	4560	1140
3	10^{-6}	$1.500\cdot10^3$	$3.789\cdot10^{-3}$		$1.880\cdot10^3$	$-5.721\cdot10^{-3}$		$4.943\cdot10^{-6}$	1222	4888	1222
4	10^{-7}	$1.500\cdot10^3$	$-6.731\cdot10^{-4}$		$1.880\cdot10^3$	$9.699\cdot10^{-4}$		$4.948\cdot10^{-6}$	1192	4768	1192
5	10^{-6}	$1.500\cdot10^3$	$6.329\cdot10^{-5}$		$1.880\cdot10^3$	$-3.749\cdot10^{-3}$		$4.900\cdot10^{-6}$	1125	4500	1125
6	10^{-7}	$1.500\cdot10^3$	$-8.378\cdot10^{-4}$		$1.880\cdot10^3$	$1.526\cdot10^{-3}$		$4.753\cdot10^{-6}$	1067	4268	1067
7	10^{-8}	$1.500\cdot10^3$	$-2.924\cdot10^{-3}$		$1.880\cdot10^3$	$1.270\cdot10^{-2}$		$5.059\cdot10^{-6}$	1144	4576	1144
8	10^{-7}	$1.500\cdot10^3$	$4.781\cdot10^{-3}$		$1.880\cdot10^3$	$-1.702\cdot10^{-2}$		$4.852\cdot10^{-6}$	1201	4804	1201
final:	0.0	$1.500\cdot10^3$	$-1.027\cdot10^{-3}$	$2.818\cdot10^2$	$1.880\cdot10^3$	$5.445\cdot10^{-3}$	$1.557\cdot10^2$	$4.803\cdot10^{-6}$	1214	4856	1214

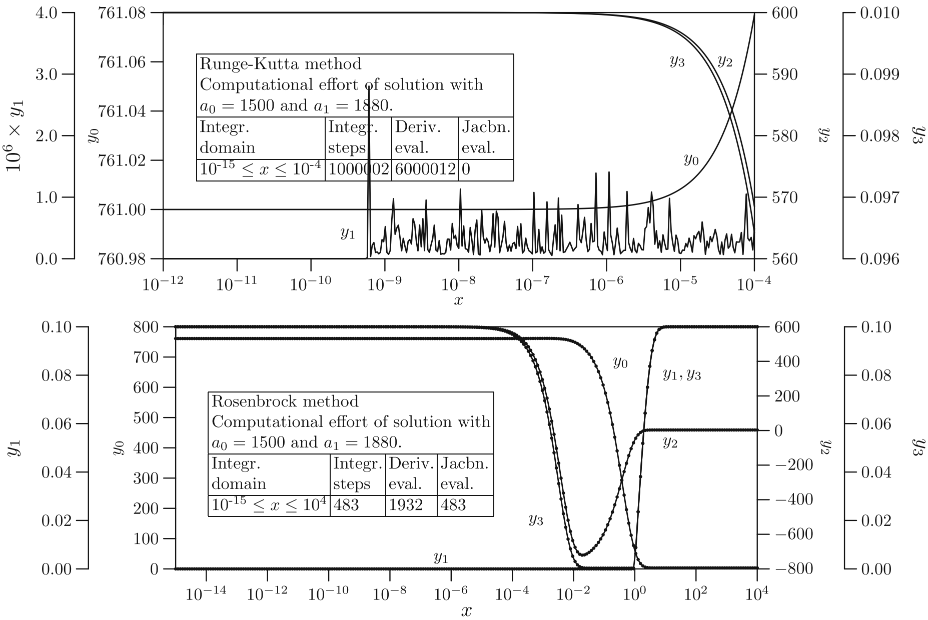

Fig. 3 Iteration-tableau of the extended Levenberg–Marquardt method with the Rosenbrock method when applied to fit system (31) to a synthetic data-set. Initial conditions from perturbation (89)–(91). Prerequisites (Algorithm 1): `maxits` $= 9$, $\tilde{\chi}^2_{\text{crit}} = 10^{-9}$, $\lambda = 10^{-3}$, $h_{\min} = 10^{-30}$, $\epsilon^{\text{rel}} = 10^{-3}$, and $\epsilon^{\text{abs}}_j = 10^{-6}$

computation is overtaken by numerical instability. The Rosenbrock method is able to compute the solution over the entire domain ($10^{-15} \leq x \leq 10^4$) with only 483 steps and 1,932 derivative evaluations, and, without becoming unstable.

3 Models for the Pressure Development of Confined Deflagrations

Two models for the pressure development of confined deflagrations are applied here. Detailed derivations of these models may be found in [28–30]. The first model, the so called thin-flame-model, assumes a flame zone of zero thickness and can be stated as:

$$\frac{dP}{dt} = 3\,(P_{\max} - P_0)\left(\frac{4\pi}{3\,V_v}\right)^{\frac{1}{3}}\left[1 - \left(\frac{P_0}{P}\right)^{\frac{1}{\gamma}}\frac{P_{\max} - P}{P_{\max} - P_0}\right]^{\frac{2}{3}}\left(\frac{P}{P_0}\right)^{\frac{1}{\gamma}} S_u \tag{32}$$

where P_0 denotes the initial pressure, $P_{\max}$ the maximum explosion pressure, γ the specific heat ratio, V_v the volume of the explosion vessel, and, S_u the burning velocity which may either be a laminar burning velocity S_{uL} or a turbulent burning velocity S_{uT}. For confined explosions the laminar burning velocity S_{uL} can be modelled as a function of the pressure by:

$$\frac{S_{uL}}{S_{uL}^{\circ}} = \left(\frac{P}{P_0}\right)^{\beta} \tag{33}$$

where $\beta = 0.6$ for hydrogen-air mixtures [30] and $\beta = 0.13$ for methane-air mixtures [29]. The model constituted by Eqs. 32 and 33 will be applied to the pressure-time traces of the laminar hydrogen-air and methane-air deflagrations.

The second model, the so called three-zone-model, assumes a flame zone of non-zero thickness, δ. For a fully developed flame, this model may be stated as

$$\frac{dP}{dt} = \frac{P_{\max} - P_0}{V_v}\left(\frac{P}{P_0}\right)^{\frac{1}{\gamma}}\frac{4\pi}{3} S_u \left[\frac{r_f^3 - r_r^3}{\delta}\right] \tag{34}$$

where S_u the burning velocity (either laminar, S_{uL}, or, turbulent, S_{uT}), δ the flame thickness (either laminar, δ_L, or turbulent, δ_T), r_f the front boundary of the flame, and, r_r the rear boundary of the flame. Explicit expressions for the flame boundaries r_r and r_f may be obtained by solving Eq. 26 of [28] to obtain:

$$r_f = \frac{\delta}{2} + \frac{3^{1/3}}{6}\left(9a + \sqrt{3}\sqrt{27a^2 + \delta^6}\right)^{1/3} - \frac{(3^{1/3}\,\delta)^2}{6\left(9a + \sqrt{3}\sqrt{27a^2 + \delta^6}\right)^{1/3}} \tag{35}$$

$$r_r = r_f - \delta \tag{36}$$

where

$$a = \frac{3V_v}{\pi}\left[1 - \left(\frac{P_0}{P}\right)^{\frac{1}{\gamma}}\frac{P_{\max} - P}{P_{\max} - P_0}\right] \tag{37}$$

Laminar flame propagation can be modelled by a set of two equations [29], one for $S_u = S_{uL}$ and one for $\delta = \delta_L$:

$$\frac{S_{uL}}{S_{uL}^{\circ}} = \left(\frac{P}{P_0}\right)^{c+\frac{\gamma-1}{\gamma}-1+\alpha} \tag{38}$$

$$\frac{\delta_L}{\delta_L^{\circ}} = \left(\frac{P}{P_0}\right)^{c-\alpha} \tag{39}$$

Here S_{uL}° and δ_L° denote the laminar burning velocity and laminar flame thickness at reference conditions of pressure and temperature. The constants c and α are substance specific and can be estimated from the temperature exponent of the laminar burning velocity using Eq. 81 from [29]. With a temperature exponent of 1.89 [29] it is seen that $c = 0.25$ for a stoichiometric methane-air mixture. With a temperature exponent of 1.4 [30], $c = 0.11$ for a stoichiometric hydrogen-air mixture. A comparison between Eqs. 38 and 33 then reveals that $\alpha = 0.59$ for a stoichiometric methane-air mixture and $\alpha = 1.2$ for a stoichiometric hydrogen-air mixture. The model constituted by Eqs. 34–39 will be applied to the pressure-time traces of the laminar hydrogen-air and methane-air deflagrations.

For turbulent flame propagation, i.e. $S_u = S_{uT}$ and $\delta = \delta_T$, four additional equations are needed, namely, one for the turbulent burning velocity (Eq. 40), one for the turbulent flame thickness (Eq. 41), one for the turbulence intensity (Eq. 42), and, one for the turbulence length scale (Eq. 43):

$$\frac{S_{uT}}{S_{uL}} = 1 + C'\mathrm{Da}^{a'}\left(\frac{v'_{\mathrm{rms}}}{S_{uL}}\right)^{b'} \tag{40}$$

$$\frac{\delta_T}{\delta_L} = 1 + C''\mathrm{Da}^{a''}\left(\frac{\ell_t}{\delta_L}\right)^{b''} \tag{41}$$

$$\frac{v'_{\mathrm{rms}}}{v^{\circ}_{\mathrm{rms}}} = \left(\frac{t}{t_0}\right)^{n} \tag{42}$$

$$\ln\left[\frac{\ell_t}{\ell_t^{\circ}}\right] = a_1 \ln\left(\frac{t}{t_0}\right) + a_2\left[\ln\left(\frac{t}{t_0}\right)\right]^2 \tag{43}$$

The constants in Eq. 42 are [31]: $t_0 = 60.0 \cdot 10^{-3}$ (s), $v^{\circ}_{\mathrm{rms}} = 3.75\ \mathrm{m\,s^{-1}}$ and $n = -1.61$. The constants in Eq. 43 are [32, 33]: $t_0 = 58.8 \cdot 10^{-3}$ (s), $\ell_t{}^{\circ} = 12.845 \cdot 10^{-3}$ m, $a_1 = -3.542$ and $a_2 = 1.321$. The values of C', C'', a', b', a'' and b'' in Eqs. 40 and 41 are addressed in Section 4. The model constituted by Eqs. 34–43 will be applied to the pressure-time trace of the turbulent methane-air deflagration in a standard 20-litre explosion sphere. Equations 42 and 43 are specific to the decaying turbulent flow field in a standard 20-litre explosion sphere. Figure 4 shows a comparison between these correlations, and, experimental v'_{rms} and ℓ_t data.

Heat losses near the wall, changes in the shape of a relatively slowly rising flame ball, or, turbulence modification that accompanies pressure and temperature variations during flame propagation, are not explicitly taken into account by this

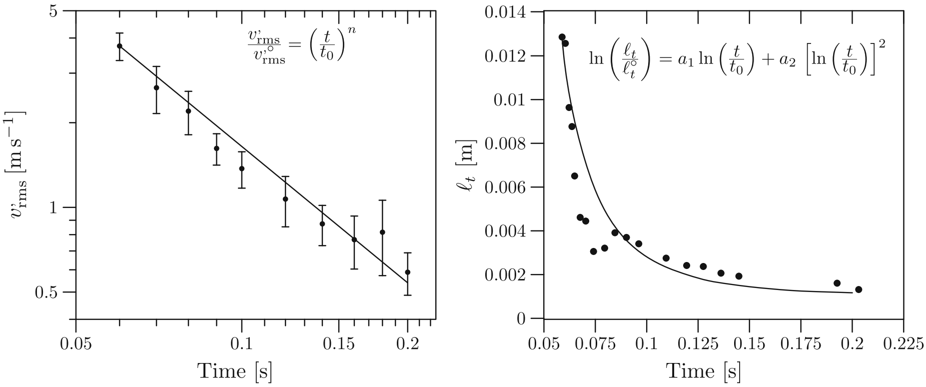

Fig. 4 Decay of the turbulence intensity, v'_{rms}, and the macro length scale, ℓ_t, in the standard 20-litre explosion sphere [31, 32]

model. Such effects are implicitly present in parameter values obtained by least-squares fitting.

4 Models for the Turbulent Burning Velocity and Flame Thickness

The availability of a satisfactory correlation for the turbulent burning velocity is of crucial importance to determine the laminar burning velocity from the pressure-time trace of a turbulent deflagration. Table 1 shows a compilation of several turbulent burning velocity models proposed over the period 1940–2012. This is merely a subset of all that could be found in the literature. Similar compilations may be found in [36–38]. To assess the applicability of these models, a comparison was made between their predictions and experimental turbulent burning velocities of a 9.52 vol % methane-air mixture and a 40 vol % hydrogen-air mixture in a fan-stirred explosion bomb [34]. The reason for selecting these data is that, in addition to experimental turbulent burning velocities in a nearly isotropic turbulent flow field, the turbulence intensity, v'_{rms}, and the turbulence macro length scale, ℓ_t, are also measured. The latter quantities must be known quantitatively to predict the turbulent burning velocity by the models in Table 1. Figure 5 shows an inter-comparison between various models in Table 1. These were computed using the following inputs.

- For the 9.52 vol % methane-air mixture: fractal dimension $D = 7/3$, $S_{uL} = 0.37$ m s^{-1} [30], $\delta_L = 1$ mm [39–41], $\mathrm{Le}_{CH_4} = 0.975$ [34], $\rho = 1.1226$ kg m^{-3}, $\mu = 1.80 \cdot 10^{-5}$ kg m^{-1} s^{-1}.
- For the 40 vol % hydrogen-air mixture: fractal dimension $D = 7/3$, $S_{uL} = 2.64$ m s^{-1}, $\delta_L = 351.8$ μm, $\mathrm{Le}_{H_2} = 3.23$ [34], $\rho = 0.736$ kg m^{-3}, $\mu = 1.81 \cdot 10^{-5}$ kg m^{-1} s^{-1}. S_{uL} and δ_L were obtained by solving the instantaneous governing Eqs. 50–53 for a 40 vol % hydrogen-air mixture with the kinetic scheme given in Fig. 6.

It is seen that no two models render the same results. Large differences exist between the predicted turbulent burning velocities. The same figure also contains a compilation of experimental turbulent burning velocities [34]. The scatter in the

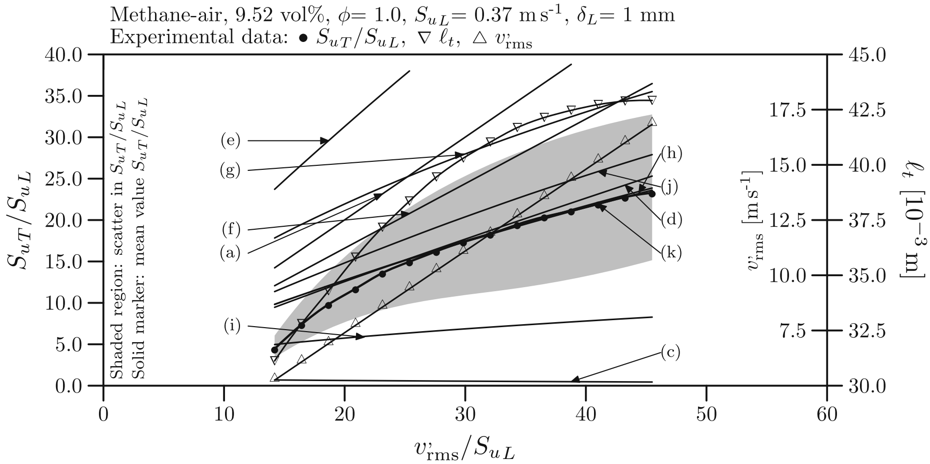

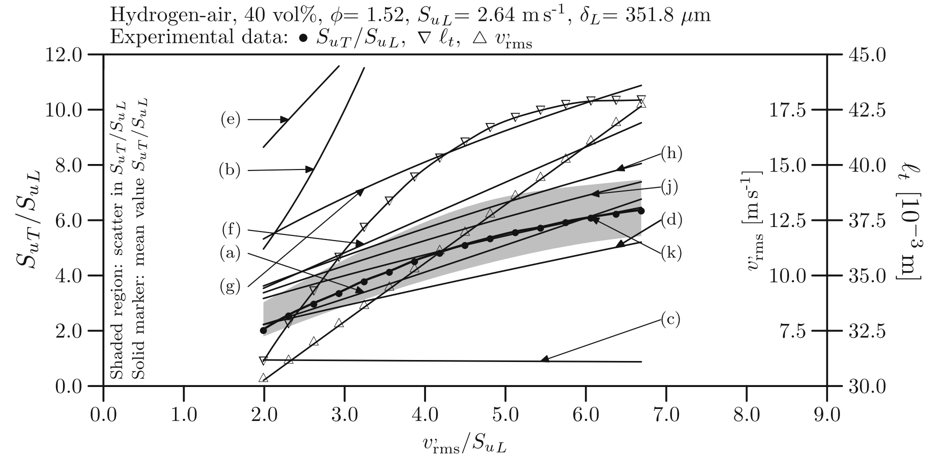

Fig. 5 Comparison between models listed in Table 1 and experimental turbulent burning velocities measured in a fan-stirred explosion bomb [34]. Inputs needed to compute the models are given in the text. *Key*: **a** Eq. 2, **b** Eq. 8, **c** Eq. 14, **d** Eq. 16, **e** Eq. 18, **f** Eq. 19, **g** Eq. 20, **h** Eq. 21, **i** Eq. 22, **j** Eq. 23, **k** Eq. 40

experimental data is indicated by the shaded region. Mean values are indicated by solid markers, connected by a solid line. A comparison with the experimental data reveals that none of the models is able to predict turbulent burning velocities that coincide with the mean values. At best only some of the models are able to produce values that fall within the experimental data scatter. This obscures the choice of a satisfactory turbulent flame propagation model.

Given the aforementioned, it is attempted here to apply the turbulent flame propagation model defined by Eqs. 40 and 41. This model may be obtained via dimensional analysis by expressing the departure of the turbulent velocity from the laminar burning velocity, $S_{uT} - S_{uL}$, as a function of the laminar burning velocity S_{uL}, the laminar flame thickness δ_L, the root-mean-square value of the velocity fluctuations v'_{rms}, the turbulence macro length scale ℓ_t, the density ρ, the dynamic

The reaction rate coefficients are in the form $k_f = \mathrm{A}T^{\beta}\exp\left(-\mathrm{E_a}/\mathrm{R}T\right)$. Units are in moles, cubic centimetres, seconds, Kelvins and calories.				
	Reaction	A	β	$\mathrm{E_a}$
1	$H_2 + O_2 \rightleftharpoons 2OH$	$1.70 \cdot 10^{13}$	0.0	47780.
2	$OH + H_2 \rightleftharpoons H_2O + H$	$1.17 \cdot 10^{9}$	1.3	3626.
3	$H + O_2 \rightleftharpoons OH + O$	$5.13 \cdot 10^{16}$	-0.816	16507.
4	$O + H_2 \rightleftharpoons OH + H$	$1.80 \cdot 10^{10}$	1.0	8826.
5	$H + O_2 + M \rightleftharpoons HO_2 + M^a$	$2.10 \cdot 10^{18}$	-1.0	0.
6	$H + O_2 + O_2 \rightleftharpoons HO_2 + O_2$	$6.70 \cdot 10^{19}$	-1.42	0.
7	$H + O_2 + N_2 \rightleftharpoons HO_2 + N_2$	$6.70 \cdot 10^{19}$	-1.42	0.
8	$OH + HO_2 \rightleftharpoons H_2O + O_2$	$5.00 \cdot 10^{13}$	0.0	1000.
9	$H + HO_2 \rightleftharpoons 2OH$	$2.50 \cdot 10^{14}$	0.0	1900.
10	$O + HO_2 \rightleftharpoons O_2 + OH$	$4.80 \cdot 10^{13}$	0.0	1000.
11	$2OH \rightleftharpoons O + H_2O$	$6.00 \cdot 10^{8}$	1.3	0.
12	$H_2 + M \rightleftharpoons H + H + M^b$	$2.23 \cdot 10^{12}$	0.5	92600.
13	$O_2 + M \rightleftharpoons O + O + M$	$1.85 \cdot 10^{11}$	0.5	95560.
14	$H + OH + M \rightleftharpoons H_2O + M^c$	$7.50 \cdot 10^{23}$	-2.6	0.
15	$H + HO_2 \rightleftharpoons H_2 + O_2$	$2.50 \cdot 10^{13}$	0.0	700.
16	$HO_2 + HO_2 \rightleftharpoons H_2O_2 + O_2$	$2.00 \cdot 10^{12}$	0.0	0.
17	$H_2O_2 + M \rightleftharpoons OH + OH + M$	$1.30 \cdot 10^{17}$	0.0	45500.
18	$H_2O_2 + H \rightleftharpoons HO_2 + H_2$	$1.60 \cdot 10^{12}$	0.0	3800.
19	$H_2O_2 + OH \rightleftharpoons H_2O + HO_2$	$1.00 \cdot 10^{13}$	0.0	1800.

[a] Third body efficiencies: $k_5(H_2O) = 21\,k_5(Ar)$, $k_5(H_2) = 3.3\,k_5(Ar)$. [b]Third body efficiencies: $k_{12}(H_2O) = 6\,k_{12}(Ar)$, $k_{12}(H) = 2\,k_{12}(Ar)$, $k_{12}(H_2) = 3\,k_{12}(Ar)$. [c] Third body efficiency: $k_{14}(H_2O) = 20\,k_{14}(Ar)$.

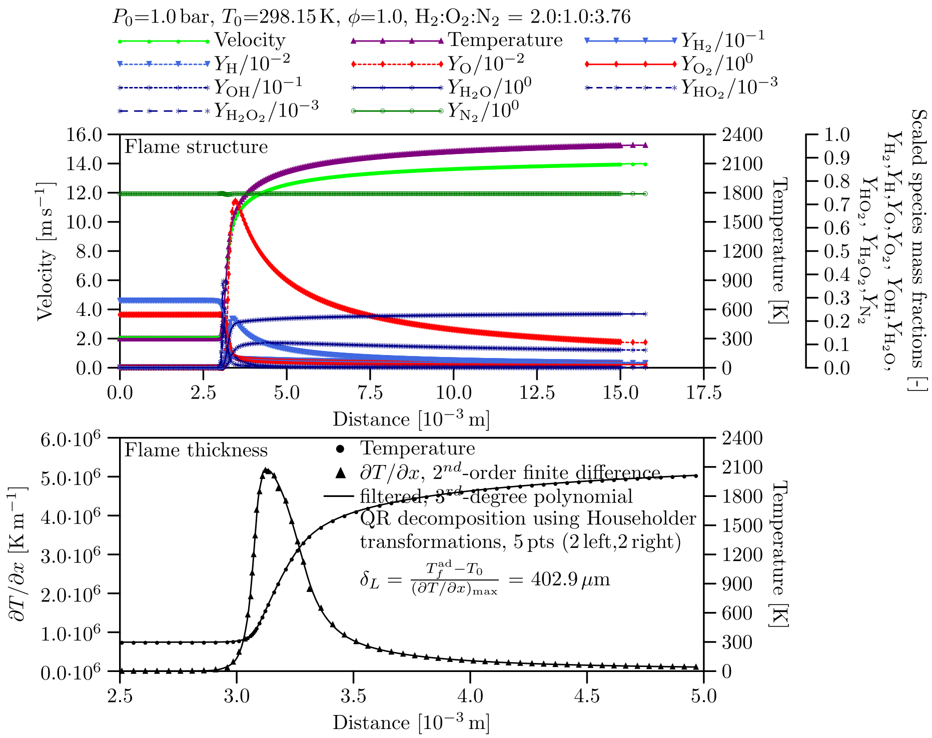

Fig. 6 Reaction mechanism [35] for hydrogen-air combustion, numerical solution of Eqs. 50–53 for velocity, temperature and species profiles across the flame zone ($\phi = 1.0$, $S_{u}{}_L^{\circ}$=2.106 m s^{-1}, initial conditions: 1 bar and 298.15 K), and, determination of laminar flame thickness from temperature profile ($T_f^{\mathrm{ad}} = 2386.3$ K, $\delta_L^{\circ} = 402.9\ \mu$m)

viscosity μ, the diffusion coefficient $\mathcal{D}$, the thermal conductivity λ, the specific heat $\hat{C}_P$, the radiant flux q_0 at a reference temperature T_0, the pressure p, the reference temperature T_0 and the gravitational acceleration g:

$$S_{uT} - S_{uL} = f\left(S_{uL}, \delta_L, v'_{\rm rms}, \ell_t, \rho, \mu, \mathcal{D}, \lambda, \hat{C}_P, q_0, p, T_0, g\right) \tag{44}$$

$$= D'\left[S_{uL}\right]^a \left[\delta_L\right]^b \left[v'_{\rm rms}\right]^c \left[\ell_t\right]^d \left[\rho\right]^e \left[\mu\right]^f \left[\mathcal{D}\right]^g \left[\lambda\right]^h \left[\hat{C}_P\right]^i \left[q_0\right]^j \left[p\right]^k \left[T_0\right]^l \left[g\right]^m \tag{45}$$

Invoking the dimensions of the quantities involved and solving system (45) for dimensional homogeneity results in $a = 1 - c - f - g - h - 3j - 2k - 2l - 2m$, $b = -d - f - g - h + m$, $e = -f - h - j - k$ and $i = -h + l$. Hence,

$$\begin{aligned}\frac{S_{uT} - S_{uL}}{S_{uL}} &= D'\left(\frac{S_{uL}\delta_L}{\mathcal{D}}\right)^{f-g-h}\left(\frac{\mu}{\rho\mathcal{D}}\right)^f\left(\frac{\lambda}{\rho\hat{C}_P\mathcal{D}}\right)^h\left(\frac{\rho S_{uL}\hat{C}_P T_0}{q_0}\right)^{-j}\\ &\quad\times\left(\frac{S_{uL}}{\sqrt{p/\rho}}\right)^{-2k}\left(\frac{S_{uL}^2}{\hat{C}_P T_0}\right)^{-l-j}\left(\frac{S_{uL}^2}{g\delta_L}\right)^{-m}\left(\frac{\ell_t/v'_{\rm rms}}{\delta_L/S_{uL}}\right)^d\left(\frac{v'_{\rm rms}}{S_{uL}}\right)^{c+d}\\ &\Longrightarrow \boxed{\frac{S_{uT}}{S_{uL}} = 1 + D'{\rm Bo}^{c'}{\rm Sc}^{d'}{\rm Le}^{e'}{\rm Bz}^{f'}{\rm Ma}^{g'}{\rm Ec}^{h'}{\rm Fr}^{i'}{\rm Da}^{a'}\left(\frac{v'_{\rm rms}}{S_{uL}}\right)^{b'}}\end{aligned} \tag{46}$$

where Bo denotes the Bodenstein number, Sc the Schmidt number, Le the Lewis number, Bz the Boltzmann number, Ma the newtonian Mach number, Ec the Eckert number, Fr the Froude number and, Da the Damköhler number.

A similar analysis can also be made for the departure of the turbulent flame thickness from the laminar flame thickness, $\delta_T - \delta_L$:

$$\delta_T - \delta_L = f\left(S_{uL}, \delta_L, v'_{\rm rms}, \ell_t, \rho, \mu, \mathcal{D}, \lambda, \hat{C}_P, q_0, p, T_0, g\right) \tag{47}$$

$$= D''\left[S_{uL}\right]^a \left[\delta_L\right]^b \left[v'_{\rm rms}\right]^c \left[\ell_t\right]^d \left[\rho\right]^e \left[\mu\right]^f \left[\mathcal{D}\right]^g \left[\lambda\right]^h \left[\hat{C}_P\right]^i \left[q_0\right]^j \left[p\right]^k \left[T_0\right]^l \left[g\right]^m \tag{48}$$

Henceforth, $a = -c - f - g - h - 3j - 2k - 2l - 2m$, $b = 1 - d - f - g - h + m$, $e = -f - h - j - k$ and $i = -h + l$ so that

$$\begin{aligned}\frac{\delta_T - \delta_L}{\delta_L} &= D''\left(\frac{S_{uL}\delta_L}{\mathcal{D}}\right)^{f-g-h}\left(\frac{\mu}{\rho\mathcal{D}}\right)^f\left(\frac{\lambda}{\rho\hat{C}_P\mathcal{D}}\right)^h\left(\frac{\rho S_{uL}\hat{C}_P T_0}{q_0}\right)^{-j}\\ &\quad\times\left(\frac{S_{uL}}{\sqrt{p/\rho}}\right)^{-2k}\left(\frac{S_{uL}^2}{\hat{C}_P T_0}\right)^{-l-j}\left(\frac{S_{uL}^2}{g\delta_L}\right)^{-m}\left(\frac{\ell_t/v'_{\rm rms}}{\delta_L/S_{uL}}\right)^{-c}\left(\frac{\ell_t}{\delta_L}\right)^{c+d}\\ &\Longrightarrow \boxed{\frac{\delta_T}{\delta_L} = 1 + D''{\rm Bo}^{c''}{\rm Sc}^{d''}{\rm Le}^{e''}{\rm Bz}^{f''}{\rm Ma}^{g''}{\rm Ec}^{h''}{\rm Fr}^{i''}{\rm Da}^{a''}\left(\frac{\ell_t}{\delta_L}\right)^{b''}}\end{aligned} \tag{49}$$

Together, Eqs. 46 and 49 constitute a turbulent flame propagation model with twenty constants: a', a'', b', b'', c', c'', d', d'', e', e'', f', f'', g', g'', h', h'', i', i'',

D' and D''. This model may be simplified into Eqs. 40 and 41 where C' and C'' are composition specific factors equal to $C' = D'\mathrm{Bo}^{c'}\mathrm{Sc}^{d'}\mathrm{Le}^{e'}\mathrm{Bz}^{f'}\mathrm{Ma}^{g'}\mathrm{Ec}^{h'}\mathrm{Fr}^{i'}$ and $C'' = D''\mathrm{Bo}^{c''}\mathrm{Sc}^{d''}\mathrm{Le}^{e''}\mathrm{Bz}^{f''}\mathrm{Ma}^{g''}\mathrm{Ec}^{h''}\mathrm{Fr}^{i''}$. Although dimensional analysis does not reveal anything about the value of D' and D'', experience shows that such constants are equal to unity when the set of inter-dependent quantities is complete and when the functional dependence on each dimensionless group is a power-law.

The completeness of the set of inter-dependent quantities may be inferred from the instantaneous governing equations for mass, species, momentum and energy. When these equations are restated in dimensionless form (see Eqs. 149–167 of [33] for details) by means of a length scale, $\mathcal{L}$, a velocity scale, $\mathcal{U}$, and, a chemical time scale, τ_c, the result becomes

$$\frac{\partial \rho^*}{\partial t^*} + \nabla^* \cdot \left(\rho^* \boldsymbol{v}^*\right) = 0 \tag{50}$$

$$\frac{\partial \left(\rho^* \boldsymbol{v}^*\right)}{\partial t^*} + \nabla^* \cdot \left(\rho^* \boldsymbol{v}^* \boldsymbol{v}^*\right) = -\mathrm{Ma}^2 \nabla^* p^* + \frac{\mathrm{Ma}^2}{\mathrm{Re}} \nabla^* \cdot \boldsymbol{\tau}^* + \frac{1}{\mathrm{Fr}} \sum_{i=1}^{N} \rho^* Y_i \boldsymbol{f}_i^* \tag{51}$$

$$\frac{\partial \left(\rho^* Y_i\right)}{\partial t^*} + \nabla^* \cdot \left(\rho^* \boldsymbol{v}^* Y_i\right) = \frac{1}{\mathrm{Re}\,\mathrm{Sc}_i} \nabla^{*2} Y_i + \mathrm{Ma}^2 \mathrm{Da}\, \dot{w}_i^* \tag{52}$$

$$\begin{aligned} \frac{\partial \left(\rho^* h^*\right)}{\partial t^*} + \nabla^* \cdot \left(\rho^* \boldsymbol{v}^* h^*\right) = \mathrm{Ma}^2 \mathrm{Ec} \left[\frac{\partial p^*}{\partial t^*} + \boldsymbol{v}^* \cdot \nabla^* p^*\right] + \frac{\mathrm{Ma}^2 \mathrm{Ec}}{\mathrm{Re}} \boldsymbol{\tau}^* : \nabla^* \boldsymbol{v}^* \\ + \frac{\mathrm{Ma}^2}{\mathrm{Re}\,\mathrm{Pr}} \nabla^{*2} T^* - \frac{\mathrm{Ma}^2}{\mathrm{Bz}} \nabla^* \cdot \boldsymbol{q}^* \\ - \frac{1}{\mathrm{Re}\,\mathrm{Sc}_i\,\mathrm{Fr}} \sum_{i=1}^{N} \rho^* Y_i \boldsymbol{f}_i^* \cdot \nabla^* Y_i \end{aligned} \tag{53}$$

Notice that $\mathrm{Le} = \mathrm{Sc}/\mathrm{Pr}$ where Pr denotes the Prandtl number, and, that $\mathrm{Bo} = \mathrm{ReSc}$ where Re denotes the Reynolds number. All non-dimensional groups in system (50)–(53), namely {Bz, Da, Ec, Fr, Ma, Pr, Re, Sc}, are covered by those appearing in correlations Eqs. 46 and 49, namely {Bo, Bz, Da, Ec, Fr, Le, Ma, Sc}.

The dimensional analysis Eqs. 44–49 reveals that the constants $\{a', b', a'', b''\}$ in Eqs. 40 and 41 are not independent from each other. They are inter-related via $b'' = b' = c + d$, $a' = d$ and $a'' = -c$. Equations 46 and 49 also show that $c'' = c' = f - g - h$, $d'' = d' = f$, $e'' = e' = h$, $f'' = f' = -j$, $g'' = g' = -2k$, $h'' = h' = -1 - j$ and $i'' = i' = -m$ which implies that the constants C' and C'' have identical dependencies on {Bo, Sc, Le, Bz, Ma, Ec, Fr}. Since $D'' = D' = 1$, this implies that $C'' = C'$. It is also worthwhile to notice that $\{c', c'', e', e'', f', f'', g', g'', h', h'', i', i''\}$ do not depend on $\{c, d\}$. Effects of physical/chemical properties on S_{uT} and δ_T are therefore singled out into C' and C'' while the influence of flow properties ($v'_{\mathrm{rms}}, \ell_t$) is captured via $\{a', a'', b', b''\}$.

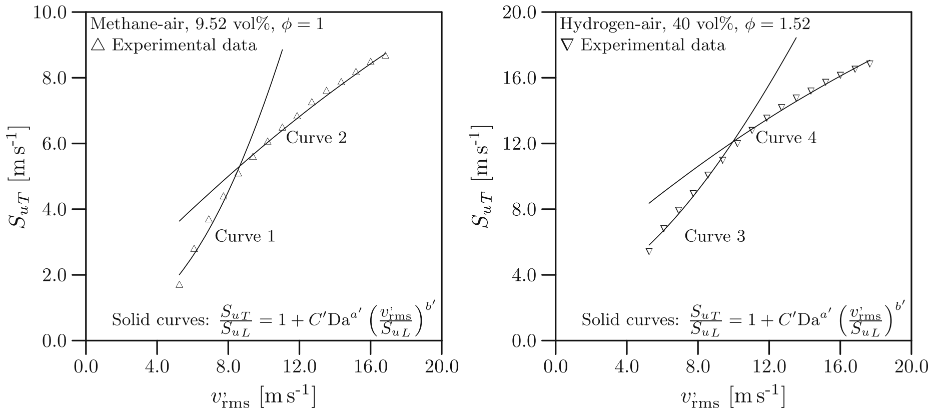

Fig. 7 Application of Eq. 40 to experimental mean turbulent burning velocities [34] in Fig. 5. The value of C', a' and b' for each curve is given in the text

A comparison of Eq. 40 with Eqs. 18–23 in Table 1 indicates that $a' = 1/4$. The values of $\{C', b', C'', a'', b''\}$ may then be found by curve-fitting Eq. 40 to the experimental data in Fig. 5. This is done in Fig. 7. It appears that there are two combustion regimes where $\{C', a', b', C'', a'', b''\}$ assume distinct values.

- For the turbulent methane-air mixture $\{C' = (6.65 \pm 0.99) \cdot 10^{-3}, a' = 1/4, b' = 2.376 \pm 0.049, C'' = 6.65 \cdot 10^{-3}, a'' = -2.13, b'' = 2.38\}$ when $5.25\,\mathrm{m\,s^{-1}} \leq v'_{\mathrm{rms}} \leq 8.56\,\mathrm{m\,s^{-1}}$ (Curve 1) and $\{C' = (0.528 \pm 0.025), a' = 1/4, b' = 0.988 \pm 0.013, C'' = 0.528, a'' = -0.738, b'' = 0.988\}$ when $9.39\,\mathrm{m\,s^{-1}} \leq v'_{\mathrm{rms}} \leq 16.83\,\mathrm{m\,s^{-1}}$ (Curve 2). There is an abrupt transition in the region $8.56\,\mathrm{m\,s^{-1}} \leq v'_{\mathrm{rms}} \leq 9.39\,\mathrm{m\,s^{-1}}$.
- For the turbulent hydrogen-air mixture $\{C' = 0.129 \pm 0.006, a' = 1/4, b' = 1.87, C''=0.129, a''= -1.62, b''=1.87\}$ when $5.25\,\mathrm{m\,s^{-1}} \leq v'_{\mathrm{rms}} \leq 9.39\,\mathrm{m\,s^{-1}}$ (Curve 3) and $\{C' = 0.437 \pm 0.012, a' = 1/4, b' = 0.946 \pm 0.016, C'' = 0.437, a'' = -0.696, b'' = 0.946\}$ when $10.22\,\mathrm{m\,s^{-1}} \leq v'_{\mathrm{rms}} \leq 17.66\,\mathrm{m\,s^{-1}}$ (Curve 4). A sudden change occurs when $9.39\,\mathrm{m\,s^{-1}} \leq v'_{\mathrm{rms}} \leq 10.22\,\mathrm{m\,s^{-1}}$.

With both mixtures, the exponent b' assumes a value close to 2 in the low turbulence regime so that Eq. 40 resembles Eqs. 7, 8 and 11 in Table 1. In the high turbulence regime b' assumes a value close to 1 so that Eq. 40 bears resemblance with Eqs. 18–23 in Table 1. The three-zone model with Eq. 40 and 41 as the turbulent flame propagation model will be applied to the pressure-time trace of a turbulent methane-air deflagration, measured in a standard 20-litre explosion sphere (Section 5).

5 Determination of the Laminar Burning Velocity from the Experimental Pressure-Time Traces of Confined Deflagrations

The experimental pressure-time traces of three confined deflagrations were analysed, namely, (i) a laminar stoichiometric hydrogen-air explosion in a 169

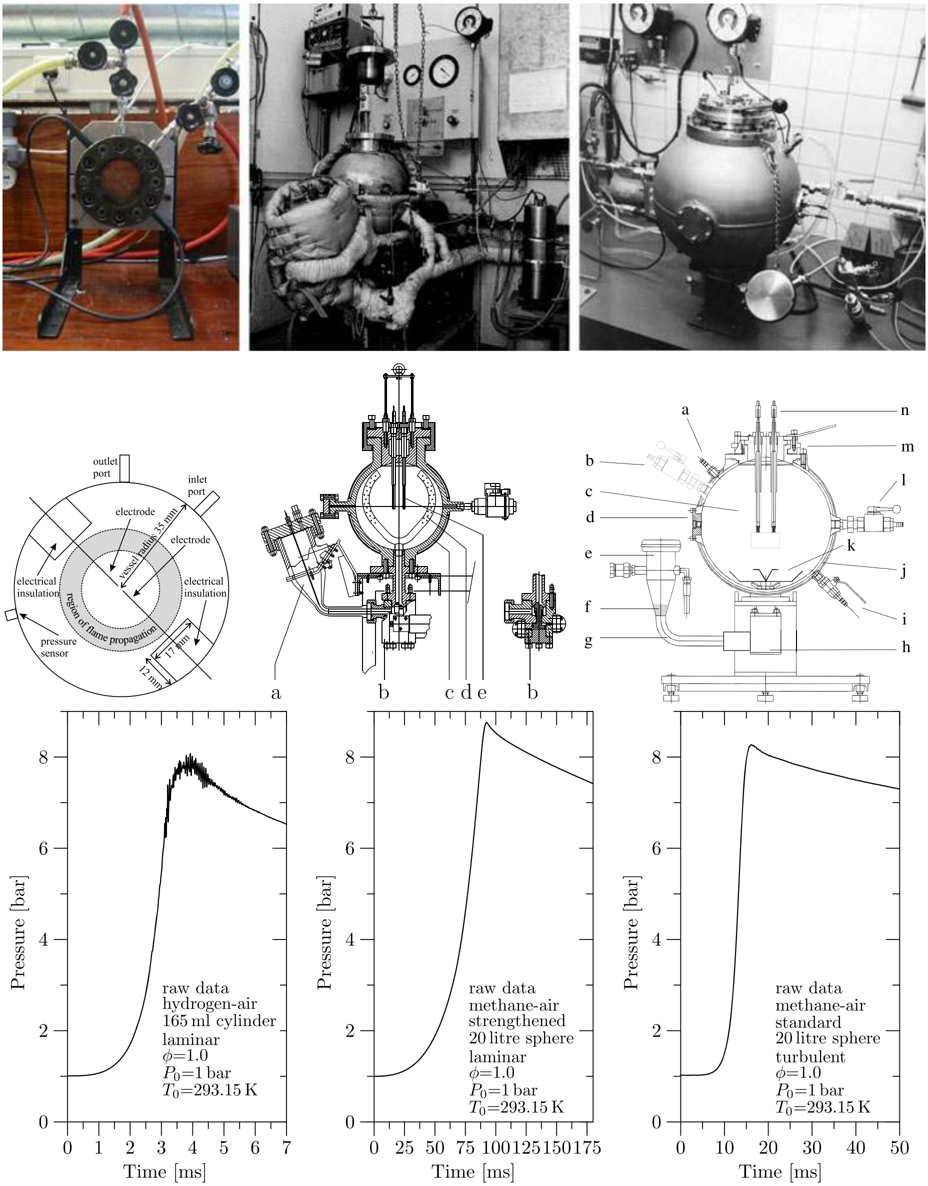

Fig. 8 Explosion equipment and pressure-time traces of hydrogen-air and methane-air deflagrations. *Upper-left* and *middle-left*: The 169 millilitre explosion cylinder [30]. *Upper-middle* and *middle-middle*: The strengthened 20-litre explosion sphere [77–79]. *Upper-right* and *middle-right*: The standard 20-litre explosion sphere [32, 80]. *Lower-left*: Pressure-time trace of a laminar stoichiometric hydrogen-air mixture in the 169 millilitre explosion cylinder. *Lower-middle*: Pressure-time trace of a laminar stoichiometric methane-air mixture in the strengthened 20-litre explosion sphere. *Lower-right*: Pressure-time trace of a turbulent stoichiometric methane-air mixture in the standard 20-litre explosion sphere

millilitre cylindrical explosion vessel [30], (ii) a laminar stoichiometric methane-air explosion in the strengthened 20-litre explosion sphere [77–79], and, (iii) a turbulent stoichiometric methane-air explosion in the standard 20-litre explosion sphere [32, 80]. The experimental equipment and pressure curves are shown in Fig. 8. All mixtures were ignited to deflagration by means of a centrally located electric spark. Details of the equipment and experimental procedures followed are given in [29, 30, 32, 77–80].

The thin-flame models (32) and (33) and the three-zone model (34)–(39) were applied to the pressure-time traces of the laminar hydrogen-air and methane-air explosions. To minimise the effect of buoyancy, to ensure a fully developed flame zone in the beginning of the dataset, and, to avoid effects of flame-wall interaction, only a subset of the pressure-time traces was used. The model-data match and the

Laminar hydrogen-air mixture, 29.5 vol%, $\phi = 1.0$						integr.	deriv.	Jacbn.
iter.	λ	$S_{u_L}^{\circ}$	$dS_{u_L}^{\circ}$	StdErr	$\tilde{\chi}^2(\boldsymbol{a})$	steps	eval.	eval.
init. guess		$2.300{\cdot}10^{0}$			$2.936{\cdot}10^{2}$	48	192	48
0	10^{-3}	$2.040{\cdot}10^{0}$	$-2.595{\cdot}10^{-1}$		$1.499{\cdot}10^{1}$	96	384	96
1	10^{-4}	$2.095{\cdot}10^{0}$	$5.407{\cdot}10^{-2}$		$1.468{\cdot}10^{1}$	96	384	96
2	10^{-5}	$2.083{\cdot}10^{0}$	$-1.138{\cdot}10^{-2}$		$1.461{\cdot}10^{1}$	96	384	96
3	10^{-6}	$2.086{\cdot}10^{0}$	$2.394{\cdot}10^{-3}$		$1.462{\cdot}10^{1}$	96	384	96
4	10^{-7}	$2.085{\cdot}10^{0}$	$-5.036{\cdot}10^{-4}$		$1.462{\cdot}10^{1}$	96	384	96
5	10^{-6}	$2.085{\cdot}10^{0}$	$1.059{\cdot}10^{-4}$		$1.462{\cdot}10^{1}$	96	384	96
final:	0.0	$2.085{\cdot}10^{0}$	$2.229{\cdot}10^{-5}$	$1.582{\cdot}10^{-2}$	$1.462{\cdot}10^{1}$	96	384	96

Laminar methane-air mixture, 9.52 vol%, $\phi = 1.0$						integr.	deriv.	Jacbn.
iter.	λ	$S_{u_L}^{\circ}$	$dS_{u_L}^{\circ}$	StdErr	$\tilde{\chi}^2(\boldsymbol{a})$	steps	eval.	eval.
init. guess		$4.500{\cdot}10^{-1}$			$4.171{\cdot}10^{4}$	298	1192	298
0	10^{-3}	$3.789{\cdot}10^{-1}$	$-7.110{\cdot}10^{-2}$		$9.262{\cdot}10^{3}$	596	2384	596
1	10^{-4}	$4.157{\cdot}10^{-1}$	$3.678{\cdot}10^{-2}$		$2.911{\cdot}10^{3}$	596	2384	596
2	10^{-5}	$3.963{\cdot}10^{-1}$	$-1.943{\cdot}10^{-2}$		$7.861{\cdot}10^{2}$	596	2384	596
3	10^{-6}	$4.064{\cdot}10^{-1}$	$1.017{\cdot}10^{-2}$		$2.723{\cdot}10^{2}$	596	2384	596
4	10^{-7}	$4.011{\cdot}10^{-1}$	$-5.346{\cdot}10^{-3}$		$1.120{\cdot}10^{2}$	596	2384	596
5	10^{-8}	$4.039{\cdot}10^{-1}$	$2.804{\cdot}10^{-3}$		$7.494{\cdot}10^{1}$	596	2384	596
final:	0.0	$4.024{\cdot}10^{-1}$	$-1.473{\cdot}10^{-3}$	$3.719{\cdot}10^{-4}$	$6.137{\cdot}10^{1}$	596	2384	596

Laminar hydrogen-air mixture, 40 vol%, $\phi = 1.52$						integr.	deriv.	Jacbn.
iter.	λ	$S_{u_L}^{\circ}$	$dS_{u_L}^{\circ}$	StdErr	$\tilde{\chi}^2(\boldsymbol{a})$	steps	eval.	eval.
init. guess		$2.300{\cdot}10^{0}$			$2.885{\cdot}10^{2}$	465	1860	465
0	10^{-3}	$2.043{\cdot}10^{0}$	$-2.574{\cdot}10^{-1}$		$2.672{\cdot}10^{1}$	860	3440	860
1	10^{-4}	$2.096{\cdot}10^{0}$	$5.357{\cdot}10^{-2}$		$1.501{\cdot}10^{1}$	788	3152	788
2	10^{-5}	$2.085{\cdot}10^{0}$	$-1.126{\cdot}10^{-2}$		$1.471{\cdot}10^{1}$	809	3236	809
3	10^{-6}	$2.087{\cdot}10^{0}$	$2.366{\cdot}10^{-3}$		$1.465{\cdot}10^{1}$	834	3336	834
4	10^{-7}	$2.087{\cdot}10^{0}$	$-4.972{\cdot}10^{-4}$		$1.465{\cdot}10^{1}$	829	3316	829
5	10^{-6}	$2.087{\cdot}10^{0}$	$1.045{\cdot}10^{-4}$		$1.465{\cdot}10^{1}$	804	3216	804
final:	0.0	$2.087{\cdot}10^{0}$	$-2.196{\cdot}10^{-5}$	$1.583{\cdot}10^{-2}$	$1.465{\cdot}10^{1}$	802	3208	802

Laminar methane-air mixture, 9.52 vol%, $\phi = 1.0$						integr.	deriv.	Jacbn.
iter.	λ	$S_{u_L}^{\circ}$	$dS_{u_L}^{\circ}$	StdErr	$\tilde{\chi}^2(\boldsymbol{a})$	steps	eval.	eval.
init. guess		$4.500{\cdot}10^{-1}$			$9.378{\cdot}10^{4}$	3363	13452	3363
0	10^{-3}	$3.514{\cdot}10^{-1}$	$-9.862{\cdot}10^{-2}$		$2.156{\cdot}10^{4}$	4148	16592	4148
1	10^{-4}	$4.064{\cdot}10^{-1}$	$5.505{\cdot}10^{-2}$		$8.674{\cdot}10^{3}$	2192	8768	2192
2	10^{-5}	$3.749{\cdot}10^{-1}$	$-3.148{\cdot}10^{-2}$		$2.503{\cdot}10^{3}$	4399	17596	4399
3	10^{-6}	$3.927{\cdot}10^{-1}$	$1.778{\cdot}10^{-2}$		$1.062{\cdot}10^{3}$	5542	22168	5542
4	10^{-7}	$3.826{\cdot}10^{-1}$	$-1.012{\cdot}10^{-2}$		$4.053{\cdot}10^{2}$	20611	82444	20611
5	10^{-8}	$3.883{\cdot}10^{-1}$	$5.734{\cdot}10^{-3}$		$2.825{\cdot}10^{2}$	8134	32536	8134
final:	0.0	$3.851{\cdot}10^{-1}$	$-3.257{\cdot}10^{-3}$	$3.559{\cdot}10^{-4}$	$1.965{\cdot}10^{2}$	743	2972	743

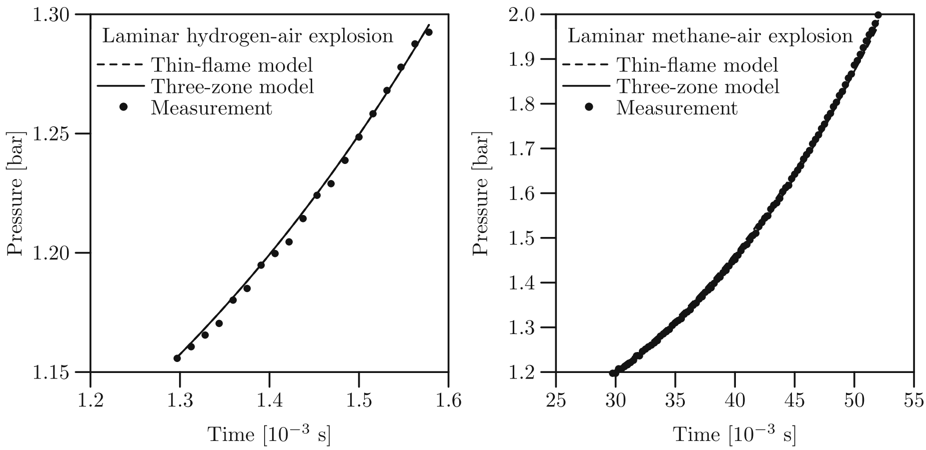

Fig. 9 Application of the thin-flame model (32) and (33) and three-zone model (34)–(39) to the experimental pressure-time traces of the laminar hydrogen-air (40 vol %, $\phi = 1.52$) and laminar methane-air (9.52 vol %, $\phi = 1.0$) explosions. Levenberg–Marquardt method with Rosenbrock method. Numerical Jacobian. Initial conditions from perturbation (89)–(91). *Upper tableaus*: thin-flame model. *Lower tableaus*: three-zone model

Turbulent methane-air mixture, 9.52 vol%, $\phi = 1.0$						integr.	deriv.	Jacbn.
iter.	λ	S_{uL}°	dS_{uL}°	StdErr	$\tilde{\chi}^2(\boldsymbol{a})$	steps	eval.	eval.
init. guess		$4.500\cdot10^{-1}$			$9.193\cdot10^{0}$	96	120	96
0	10^{-3}	$3.056\cdot10^{-1}$	$-1.444\cdot10^{-1}$		$1.697\cdot10^{1}$	184	736	184
1	10^{-2}	$3.979\cdot10^{-1}$	$9.232\cdot10^{-2}$		$2.121\cdot10^{0}$	184	736	184
2	10^{-3}	$3.602\cdot10^{-1}$	$-3.770\cdot10^{-2}$		$1.577\cdot10^{0}$	184	736	184
3	10^{-4}	$3.844\cdot10^{-1}$	$2.421\cdot10^{-2}$		$1.295\cdot10^{0}$	184	736	184
4	10^{-5}	$3.702\cdot10^{-1}$	$-1.417\cdot10^{-2}$		$1.138\cdot10^{0}$	184	736	184
5	10^{-6}	$3.791\cdot10^{-1}$	$8.892\cdot10^{-3}$		$1.142\cdot10^{0}$	184	736	184
final:	0.0	$3.738\cdot10^{-1}$	$-5.380\cdot10^{-3}$	$3.595\cdot10^{-2}$	$1.099\cdot10^{0}$	184	736	184

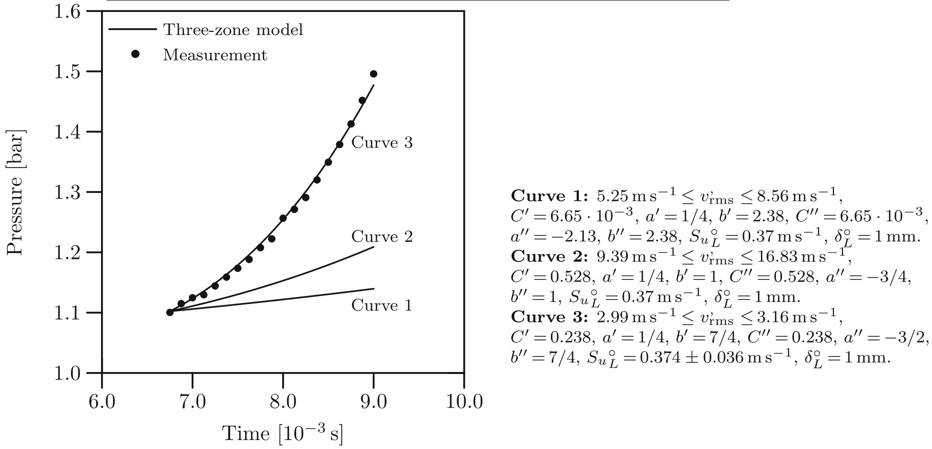

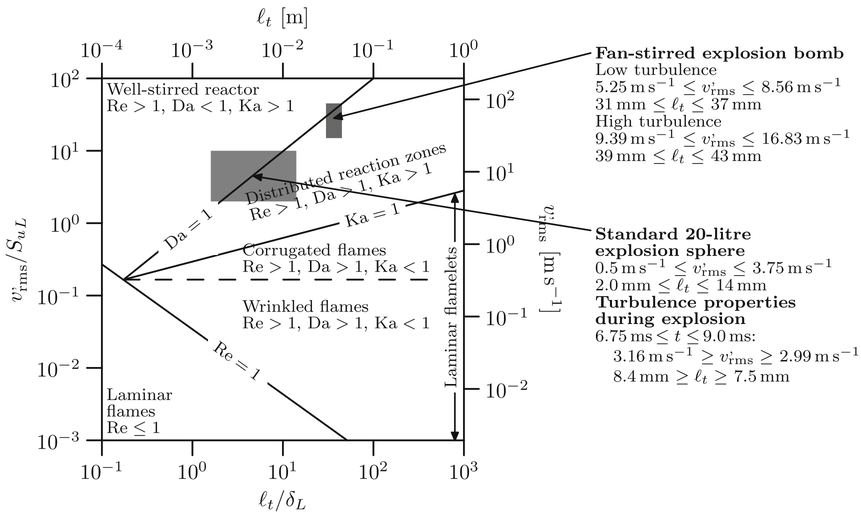

Fig. 10 Application of the three-zone model (34)–(43) to the experimental pressure-time trace of the turbulent methane-air (9.52 vol %, $\phi = 1.0$) explosion. Levenberg–Marquardt method with Rosenbrock method. Numerical Jacobian. Initial conditions from perturbation (89)–(91). *Upper-part*: Iteration-tableau and model-data match. *Lower-part*: Borghi diagram [81]

iteration-tableaus of Algorithm 1 with `maxits` $= 6$, $\tilde{\chi}^2_{\mathrm{crit}} = 10^{-3}$, $\lambda = 10^{-3}$, $h_{\mathrm{init}} = 10^{-4}$, $\epsilon^{\mathrm{rel}} = 10^{-4}$ and $\epsilon_j^{\mathrm{abs}} = 10^{1}$ are shown in Fig. 9. The laminar burning velocities obtained by the thin-flame model are: $S_{uL}^{\circ} = 2.085 \pm 0.016\ \mathrm{m\,s^{-1}}$ for the stoichiometric hydrogen-air mixture and $S_{uL}^{\circ} = 40.24 \pm 0.037\ \mathrm{cm\,s^{-1}}$ for the stoichiometric methane-air mixture. A compilation of laminar burning velocities of hydrogen-air and methane-air mixtures collected from the literature is given in [29, 30]. Laminar burning velocities in these compilations, which are believed to be the most accurate ones, have a magnitude of $S_{uL}^{\circ} = 2.1 - -2.2\ \mathrm{m\,s^{-1}}$ for the stoichiometric hydrogen-air mixture and $S_{uL}^{\circ} = 37 - -40\ \mathrm{cm\,s^{-1}}$ for the stoichiometric methane-air mixture. Both laminar burning velocities obtained by the thin-flame model are close to the values obtained from the literature. That of hydrogen-air is slightly below the lower limit and that of methane-air is slightly above the upper limit.

To apply the three-zone model (34)–(39) it was necessary to have an estimate of the laminar flame thickness, δ_L°, in Eq. 39. For stoichiometric methane-air mixtures estimates of 1 mm have been reported for δ_L° [39–41]. For hydrogen-air mixtures there are no such measurements. To find an estimate for δ_L° of the hydrogen-air mixture, the instantaneous governing Eqs. 50–53 were solved with the kinetic mechanism in Fig. 6 using the CANTERA Suite of Numerical Algorithms [82]. From the numerical solution, shown in Fig. 6, it was found that $S_{uL}^{\circ} = 2.106\ \mathrm{m\,s^{-1}}$ and $\delta_L^{\circ} = 402.9\ \mu\mathrm{m}$ for a stoichiometric hydrogen-air mixture at initial conditions of 1 bar and 298.15 K. The laminar burning velocities obtained by least-squares fitting the three-zone model (34)–(39) are: $S_{uL}^{\circ} = 2.087 \pm 0.016\ \mathrm{m\,s^{-1}}$ for the stoichiometric hydrogen-air mixture and $S_{uL}^{\circ} = 38.51 \pm 0.036\ \mathrm{cm\,s^{-1}}$ for the stoichiometric methane-air mixture. In these calculations the laminar flame thickness of hydrogen-air and methane-air were held at fixed values of $\delta_L^{\circ} = 402.9\ \mu\mathrm{m}$ and $\delta_L^{\circ} = 1$ mm. While the laminar burning velocity of the hydrogen-air mixture remains slightly below the lower limit of the range of literature values (2.1–$2.2\ \mathrm{m\,s^{-1}}$), that obtained for the methane-air mixture is seen to fall within the range of literature values (37–$40\ \mathrm{cm\,s^{-1}}$).

The three-zone model (34)–(43) was also applied to determine the laminar burning velocity from the pressure-time trace of a turbulent stoichiometric methane-air explosion in a standard 20-litre sphere. For this calculation, the prerequisites in Algorithm 1 were: $\mathtt{maxits} = 6$, $\tilde{\chi}^2_{\mathrm{crit}} = 10^{-3}$, $\lambda = 10^{-3}$, $h_{\mathrm{init}} = 10^{-4}$, $\epsilon^{\mathrm{rel}} = 10^{-4}$ and $\epsilon_j^{\mathrm{abs}} = 10^{1}$. The model-data match, illustrated by Curve 3 in Fig. 10, was obtained with the constants $\{C' = 0.238,\ a' = 1/4,\ b' = 7/4,\ C'' = 0.238,\ a'' = -3/2,\ b'' = 7/4\}$ in the turbulent flame propagation model (40) and (41). The resulting laminar burning velocity is $S_{uL}^{\circ} = 0.374 \pm 0.036\,\mathrm{m\,s^{-1}}$, which is within the range of literature values (37–$40\ \mathrm{cm\,s^{-1}}$). The same figure also shows the calculated pressure-time curves obtained with the constants belonging to Curves 1 and 2 in Fig. 7. A large discrepancy exists between these curves and the experimental data. The reasons behind, and implications of this disparity are addressed in the next section.

6 Conclusions

The classical Levenberg–Marquardt method, originally developed for algebraic models involving a single dependent variable, was extended to cope with systems of differential equations involving multiple dependent variables (Appendix C). An explicit Runge–Kutta method for non-stiff systems, and, an implicit Rosenbrock method for stiff systems were embedded into the extended method. To verify its implementation, this combination of methods was applied to three benchmark test problems, namely, systems (24)–(25), (30) and (31). Synthetic data-sets were generated for these systems with specified model parameters. In all cases, and even with the occurrence of stiffness, the extended method was able to recover the parameters with a minimal computational effort (Section 2). As a further test, two integral balance models (Section 3) were applied to experimental pressure-time traces of a laminar hydrogen-air and methane-air explosion (Fig. 9). The resulting laminar burning velocities are in agreement with literature values.

The turbulent three-zone model (34)–(43) was applied to the pressure-time trace of a stoichiometric methane-air explosion in the decaying turbulent flow field of the standard 20-litre sphere. For this it was necessary to quantify $\{C', a', b', C'', a'', b''\}$ in the Eqs. 40 and 41. A comparison between Eq. 40 and experimental data in Fig. 7 revealed that two distinct sets of constants exist within the operating conditions of the fan-stirred explosion bomb (shaded region in Fig. 10). Application of these constants to the pressure-time curve measured in the 20-litre sphere resulted in a large discrepancy (Curves 1 and 2 in Fig. 10). The reason behind this discordance is that the operating conditions of the 20-litre sphere (shaded region in Fig. 10) are very different from those in the fan-stirred bomb, and, $\{C', a', b', C'', a'', b''\}$ assume distinct values. The pressure curve measured in the 20-litre sphere can only be matched (Curve 3 in Fig. 10) with the following constants: $\{C' = 0.238, a' = 1/4, b' = 7/4, C'' = 0.238, a'' = -3/2, b'' = 7/4\}$.

The existence of disparate coefficients at different locations within the Borghi-diagram implies a consequential need for research into their values. The experimental data used in Fig. 10 are limited to a time span covering only 2.25 ms. Hence the turbulence conditions cover a very small part of the Borghi-diagram. But the operating conditions of the standard 20-litre sphere much wider (Fig. 10). The usefulness of this equipment may therefore be extended beyond its widespread application to determine practical explosion parameters. For example, combustible mixtures could be investigated at different ignition delay times to reveal more about $\{C', a', b', C'', a'', b''\}$ in other parts of the Borghi-diagram.

It must be emphasized that a spherical flame shape is pivotal to the validity of the models applied here. For a stoichiometric methane-air mixture, the turbulence conditions in the standard 20-lite sphere do not cause the flame to deviate substantially from its spherical shape within this brief time span. But when, for example, the burning velocity becomes much lower due to a lean or rich gas composition, the flame shape may deviate from the assumed spherical geometry. Optical verification of the flame shape is then required to scrutinise the applicability of the integral balance models deployed in this work.

7 Nomenclature

The symbols used throughout this paper are explained below. When a symbol represents something else than stated here, or when a symbol in the text is not explained here, or when it represents more than one quantity, its precise meaning is clarified by the text. Wherever possible and convenient we used the notation by [19, 83].

Latin Symbols		
$\hat{C}_P$	Constant pressure specific heat.	[J kg^{-1} K^{-1}]
$\boldsymbol{f}_i$	Body force $\boldsymbol{f}_i$ acting on the i-th species.	[N]
g	Gravitational acceleration g.	[m s^{-2}]
h	Microscopic enthalpy h	[J kg^{-1}]
p	Microscopic pressure.	[Pa]
P	Macroscopic pressure.	[Pa]
$P_{\max}$	Maximum explosion pressure.	[Pa]
$\boldsymbol{q}$	Radiant flux. Radiant fluxes emitted from reaction zones are often described as $\boldsymbol{q} = \epsilon\sigma T^4$ [84, p. 646] where σ denotes the Stefan–Boltzmann constant and ϵ is the emissivity.	[W m^{-2}]
r_f	Front boundary of the flame zone.	[m]
r_r	Rear boundary of the flame zone.	[m]
S_u	Burning velocity.	[m s^{-1}]
S_{uL}	Laminar burning velocity.	[m s^{-1}]
S_{uL}°	Laminar burning velocity at reference conditions.	[m s^{-1}]
S_{uT}	Turbulent burning velocity.	[m s^{-1}]
T	Temperature	[K]
$\boldsymbol{v}$	Microscopic velocity.	[m s^{-1}]
v'_{rms}	Root-mean-square value of the velocity fluctuations.	[m s^{-1}]
V_v	Volume explosion vessel	[m^3]
$\dot{w}_i$	Chemical source of the i-th species.	[kg m^{-3} s^{-1}]
Y_i	Mass fraction of the i-th species	[–]
Greek Symbols		
γ	Specific heat ratio.	[–]
δ	Flame thickness	[m]
δ_L	Laminar flame thickness	[m]
δ_L°	Laminar flame thickness at reference conditions	[m]
δ_T	Turbulent flame thickness	[m]
λ	Thermal conductivity.	[W m^{-1} K^{-1}]
λ_T	Taylor micro length scale	[m]
μ	Dynamic viscosity.	[Pa s]
ν	Kinematic viscosity.	[m^{-2} s]
ρ	Density.	[kg m^{-3}]
τ	$\tau = \mu\left(\nabla\boldsymbol{v} + (\nabla\boldsymbol{v})^{\dagger}\right) + \left(\kappa - \frac{2}{3}\mu\right)(\nabla\cdot\boldsymbol{v})\, I$ denotes the shear stress tensor. κ denotes the bulk viscosity.	[N m^{-2}]
Other Symbols		
$\mathcal{D}_i$	Fickian diffusion coefficient of the i-th species.	[m^2 s^{-1}]
Scales		
ℓ_G	Gibson length scale	[m]
ℓ_K	Kolmogorov length scale	[m]
ℓ_t	Turbulence macro length scale	[m]
$\mathcal{L}$	Length scale.	[m]
$\mathcal{M}$	Molecular mass.	[kg mol^{-1}]
τ_c	Chemical time scale.	[s]

τ_K	Kolmogorov time scale	[s]
τ_t	Turbulence macro time scale	[s]
υ_K	Kolmogorov velocity scale.	[m s^{-1}]
υ_t	Turbulence macro velocity scale.	[m s^{-1}]
$\mathcal{U}$	Velocity scale.	[m s^{-1}]
Dimensionless Independent Variables and Operators		
t^*	Physical time t over $\mathcal{L}/\mathcal{U}$.	[−]
∇^*	Nabla operator divided by the reciprocal length scale, $\nabla/\mathcal{L}^{-1}$.	[−]
Nondimensional Dependent Variables		
ρ^*	Density ρ divided by $p/\mathcal{U}^2$.	[−]
$\boldsymbol{v}^*$	Velocity $\boldsymbol{v}$ divided by the velocity scale $\mathcal{U}$.	[−]
p^*	Microscopic pressure p divided by $\rho\,\mathcal{U}^2$.	[−]
$\boldsymbol{\tau}^*$	Shear stress tensor τ, divided by $\mu\,\mathcal{U}/\mathcal{L}$.	[−]
$\boldsymbol{f}_i^*$	Body force $\boldsymbol{f}_i$ on the i-th species divided by the magnitude of the gravitational force g.	[−]
Y_i	Mass fraction of the i-th species.	[−]
$\dot{w}_i^*$	Chemical source $\dot{w}_i$ divided by $\rho(\mathcal{L}/\mathcal{U})/\tau_c$.	[−]
h^*	Enthalpy h divided by $\hat{C}_P\,T_0$.	[−]
T^*	Temperature T divided by a reference temperature T_0.	[−]
$\boldsymbol{q}^*$	Radiant flux $\boldsymbol{q}$ divided by the magnitude of the radiant energy flux q_0 at a reference temperature.	[−]
Dimensionless Groups		
Bo	Bodenstein number, $\mathcal{U}\mathcal{L}/\mathcal{D}$. Bo = Re Sc. It is the mass transfer analogue to the Peclet number, Pe.	[−]
Bz	Boltzmann number, $\rho\,\mathcal{U}\,\hat{C}_P\,T_0/q_0$.	[−]
Da	Damköhler number, $(\mathcal{L}/\mathcal{U})/\tau_c = \ell_t S_{uL}/\upsilon_t\delta_L$.	[−]
Ec	Eckert number, $\mathcal{U}^2/\hat{C}_P\,T_0$.	[−]
Fr	Froude number, $\mathcal{U}^2/g\mathcal{L}$.	[−]
Ka	Karlovitz number, $\tau_c/(\mathcal{L}/\mathcal{U}) = \upsilon_K\delta_L/\ell_K S_{uL}$.	[−]
Le$_i$	Lewis number of i-th species, $\lambda/\rho\,\hat{C}_P\mathcal{D}_i$. Le = Sc$_i$/Pr.	[−]
Ma	Newtonian Mach number, $\mathcal{U}/\sqrt{p/\rho}$.	[−]
Pe	Peclet number, $\rho\,\hat{C}_P\mathcal{U}\mathcal{L}/\lambda$. Pe = Re Pr.	[−]
Pr	Prandtl number, $\mu\,\hat{C}_P/\lambda$.	[−]
Re	Reynolds number, $\rho\,\mathcal{U}\mathcal{L}/\mu$.	[−]
Sc$_i$	Schmidt number of i-th species, $\mu/\rho\mathcal{D}_i$.	[−]

Appendix A: Least-Squares Minimisation and the Levenberg–Marquardt Method

Least-squares minimisation [19, 83, 85, 86] is a strategy whereby the parameters of a model are adjusted to obtain the closest match with a data collection. In this work the model is defined by the system

$$\boldsymbol{y}\left(\boldsymbol{a}, \boldsymbol{b}, \boldsymbol{x}, \boldsymbol{y}\right) = y_j\left(\boldsymbol{a}, \boldsymbol{b}, \boldsymbol{x}, \boldsymbol{y}\right) \qquad 0 \leq j < ny \tag{54}$$

containing ny equations. It may either consist of ny algebraic equations, or, contain the primitives of ny ordinary differential equations. With algebraic equations, the system $y_j\left(\boldsymbol{a}, \boldsymbol{b}, \boldsymbol{x}, \boldsymbol{y}\right)$ takes the form

$$y_j\left(\{a_0, \ldots, a_{ma-1}\}, \{b_0, \ldots, b_{mb-1}\}, \{x_0, \ldots, x_{nx-1}\}, \{y_0, \ldots, y_{ny-1}\} \setminus \{y_j\}\right) \tag{55}$$

with ma parameters $\boldsymbol{a} = [a_0, \ldots, a_{ma-1}]$, mb constants $\boldsymbol{b} = [b_0, \ldots, b_{mb-1}]$, nx independent variables $\boldsymbol{x} = [x_0, \ldots, x_{nx-1}]$, and, ny dependent variables $\boldsymbol{y} = [y_0, \ldots, y_{ny-1}]$. Each algebraic equation indexed by j may contain any of the dependent variables on its right hand side except for y_j. Implicit dependence of the j-th equation $y_j\left(\boldsymbol{a}, \boldsymbol{b}, \boldsymbol{x}, \boldsymbol{y}\right)$ on y_j is not permitted. If each equation in system (54) represents the antiderivative of an ordinary differential equation (cf. system (72)), there is only one independent variable x. Each member then takes the form

$$\begin{aligned} y_j\left(\boldsymbol{a}, \boldsymbol{b}, \boldsymbol{x}, \boldsymbol{y}\right) &= y_j\left(\{a_0, \ldots, a_{ma-1}\}, \{b_0, \ldots, b_{mb-1}\}, \{x\}, \{y_0, \ldots, y_{ny-1}\}\right) \\ &= \int_{x^*,\ \boldsymbol{y}^*(\boldsymbol{a},\boldsymbol{b},x^*,\boldsymbol{y}^*)}^{x,\ \boldsymbol{y}(\boldsymbol{a},\boldsymbol{b},x,\boldsymbol{y})} \frac{\partial y_j\left(\boldsymbol{a}, \boldsymbol{b}, x, \boldsymbol{y}\right)}{\partial x}\, dx \\ &= \int_{x^*,\ \boldsymbol{y}^*(\boldsymbol{a},\boldsymbol{b},x^*,\boldsymbol{y}^*)}^{x,\ \boldsymbol{y}(\boldsymbol{a},\boldsymbol{b},x,\boldsymbol{y})} f_j\left(\boldsymbol{a}, \boldsymbol{b}, x, \boldsymbol{y}\right)\, dx \end{aligned} \tag{56}$$

with ny initial conditions $[x^*,\ \boldsymbol{y}^*(\boldsymbol{a}, \boldsymbol{b}, x^*, \boldsymbol{y}^*)]$. Equation 56 makes it possible to incorporate a system of ordinary differential equations via its numerical solution.

The data collection to be matched consists of N realisations:

$$(x^i, \hat{\boldsymbol{y}}^i_j, \hat{\boldsymbol{\sigma}}^i_j) \qquad 0 \le i < N, \quad 0 \le j < ny \tag{57}$$

Each realisation $\hat{y}^i_j$ has a measurement error causing it to be scattered randomly around the mean values $\bar{y}^i_j$ that would be obtained by averageing a large number of $\hat{y}^i_j$. The scatter in $\hat{y}^i_j$ is assumed to have a Gaussian distribution with a standard deviation $\hat{\sigma}^i_j$. For a scalar function $y(\boldsymbol{a}, \boldsymbol{b}, x)$, where $\boldsymbol{a}$ denotes the parameter set to be adjusted, [19, 23, 83] define a quantity χ^2 as

$$\chi^2\left(\boldsymbol{a}, \boldsymbol{b}, x, y, \hat{y}, \hat{\sigma}\right) = \sum_{i=0}^{N-1} \left[\frac{\hat{y}^i - y(\boldsymbol{a}, \boldsymbol{b}, x^i)}{\hat{\sigma}^i}\right]^2 \tag{58}$$

The summation over i spans all realisations in the data collection (Eq. 57). A minimum in this so-called *chi-square* implies the closest match between the model $y(\boldsymbol{a}, \boldsymbol{b}, x)$ and the data collection $\left(\boldsymbol{x}^i, \hat{y}^i, \hat{\sigma}^i\right)$. The condition of a minimum in χ^2, obtained by differentiating Eq. 58 with respect to $\boldsymbol{a}$ and setting the result equal to zero, leads to a set of ma algebraic equations with ma unknowns $[a_0, \ldots, a_{ma-1}]$. Its solution yields the parameters $\boldsymbol{a}^{\min}$ that render the closest match between the model $y(\boldsymbol{a}, \boldsymbol{b}, x)$ and the data collection $\left(x^i, \hat{y}^i, \hat{\sigma}^i\right)$.

In the present work the dependent variable is not a single valued scalar but a vector $\boldsymbol{y}$ containing ny elements. This makes it necessary to modify the *chi-square*. Following [19, 23, 83], but now with the dependent variable being a vector,

$$\boldsymbol{\chi}^2\left(\boldsymbol{a}, \boldsymbol{b}, x, \boldsymbol{y}, \hat{\boldsymbol{y}}, \hat{\boldsymbol{\sigma}}\right) = \sum_{i=0}^{N-1} \left[\frac{\hat{y}^i_j - y_j(\boldsymbol{a}, \boldsymbol{b}, x^i, \boldsymbol{y})}{\hat{\sigma}^i_j}\right]^2 \qquad 0 \le j < ny \tag{59}$$

Here $\boldsymbol{\chi}^2$ is a vector containing ny elements $[\chi_0^2, \ldots, \chi_{ny-1}^2]$. But then something undesirable happens: application of the condition for a minimum in $\boldsymbol{\chi}^2$ results in an over-determined system of $ny \times ma$ equations with only ma unknowns $[a_0, \ldots, a_{ma-1}]$. To overcome this, the *chi-square* is modified here to become a scalar quantity, $\tilde{\chi}^2$, taken to be the sum of the elements of $\boldsymbol{\chi}^2$:

$$\tilde{\chi}^2 \left(\boldsymbol{a}, \boldsymbol{b}, x, \boldsymbol{y}, \hat{\boldsymbol{y}}, \hat{\boldsymbol{\sigma}}\right) = \sum_{j=0}^{ny-1} \sum_{i=0}^{N-1} \left[\frac{\hat{y}_j^i - y_j(\boldsymbol{a}, \boldsymbol{b}, x^i, \boldsymbol{y})}{\hat{\sigma}_j^i} \right]^2 \tag{60}$$

The elements of $\boldsymbol{\chi}^2$ are all positive numbers whose sum is assumed to be a global minimum at the optimal model-data match. The condition for a minimum in $\tilde{\chi}^2$ then leads to

$$0 = \sum_{j=1}^{ny-1} \sum_{i=0}^{N-1} \left[\frac{\hat{y}_j^i - y_j(\boldsymbol{a}, \boldsymbol{b}, x^i, \boldsymbol{y})}{\hat{\sigma}_j^{i2}} \right] \left[\frac{\partial y_j(\boldsymbol{a}, \boldsymbol{b}, x^i, \boldsymbol{y})}{\partial a_k} \right] \quad 0 \le k < ma \tag{61}$$

containing ma equations and ma unknowns $[a_0, \ldots, a_{ma-1}]$ so that it can be solved to find closest model-data match.

The set of algebraic Eq. 61 may be linear or non-linear in the unknowns $\boldsymbol{a}$. For a linear system there are well-established methods to compute the solution. However, if system (61) contains one or more non-linear equations then it becomes necessary to resort to procedures that approximate $\boldsymbol{a}$ iteratively. Procedures to achieve this are the gradient-descent method [86], the Gauss–Newton method [86], and, the Levenberg–Marquardt method [19, 23, 83, 85, 86] which is a hybridisation between the former two. Detailed derivations of the latter are given in [19, 83, 85, 86]. For the purpose of this paper it will suffice to consider this method on the basis of a second order Taylor expansion of $\boldsymbol{\chi}^2$ in the $\tilde{\chi}^2 - \boldsymbol{a}$ parameter space:

$$\tilde{\chi}^2(\boldsymbol{a} + d\boldsymbol{a}) = \tilde{\chi}^2\left(\boldsymbol{a}\right) + \nabla\tilde{\chi}^2\Big|_{\boldsymbol{a}} \cdot d\boldsymbol{a} + \tfrac{1}{2} d\boldsymbol{a} \cdot \nabla\nabla\tilde{\chi}^2\Big|_{\boldsymbol{a}} \cdot d\boldsymbol{a} + \ldots \tag{62}$$

This can be applied to compute $\boldsymbol{a}^{\min}$ from an initial guess $\boldsymbol{a}^{\text{cur}}$:

$$\tilde{\chi}^2(\boldsymbol{a}^{\min}) = \tilde{\chi}^2(\boldsymbol{a}^{\text{cur}}) + \nabla\tilde{\chi}^2\Big|_{\boldsymbol{a}^{\text{cur}}} \cdot d\boldsymbol{a} + \tfrac{1}{2} d\boldsymbol{a} \cdot \nabla\nabla\tilde{\chi}^2\Big|_{\boldsymbol{a}^{\text{cur}}} \cdot d\boldsymbol{a} \tag{63}$$

If the initial guess, $\boldsymbol{a}^{\text{cur}}$, is very close to $\boldsymbol{a}^{\min}$ so that $\tilde{\chi}^2(\boldsymbol{a}^{\text{cur}}) \approx \tilde{\chi}^2(\boldsymbol{a}^{\min})$ then the increment $d\boldsymbol{a}$ leading to $\boldsymbol{a}^{\min}$ may be calculated from Eq. 63 as

$$d\boldsymbol{a} = -2 \left[\nabla\nabla\tilde{\chi}^2\Big|_{\boldsymbol{a}^{\text{cur}}} \right]^{-1} \cdot \nabla\tilde{\chi}^2\Big|_{\boldsymbol{a}^{\text{cur}}} \tag{64}$$

This defines the Gauss–Newton method for solving non-linear least squares problems, and, the Newton method for calculating the roots of algebraic equation systems. Unless the initial guess, $\boldsymbol{a}^{\text{cur}}$, is very close to $\boldsymbol{a}^{\min}$ there is no guarantee that the difference between $\tilde{\chi}^2(\boldsymbol{a}^{\text{cur}})$ and $\tilde{\chi}^2(\boldsymbol{a}^{\min})$ in Eq. 63 is small enough to enable Eq. 64 to render an increment $d\boldsymbol{a}$ that improves $\boldsymbol{a}^{\text{cur}}$ to obtain $\boldsymbol{a}^{\min}$. Equation 64 will therefore only work when the initial guess $\boldsymbol{a}^{\text{cur}}$ is provided using a priori knowledge of $\boldsymbol{a}^{\min}$, or, another numerical method is applied to improve a poor initial guess. Such a procedure follows from the total differential of Eq. 63 while neglecting the third term on its right hand side (notice that $d\boldsymbol{a} = \boldsymbol{a}^{\text{next}} - \boldsymbol{a}^{\text{cur}}$):

$$d\tilde{\chi}^2(\boldsymbol{a}^{\text{next}}) = d\tilde{\chi}^2(\boldsymbol{a}^{\text{cur}}) + d\left[\nabla\tilde{\chi}^2\Big|_{\boldsymbol{a}^{\text{cur}}}\right]\cdot d\boldsymbol{a} \Longrightarrow d\boldsymbol{a} = \left[\nabla\nabla\tilde{\chi}^2\Big|_{\boldsymbol{a}^{\text{cur}}}\right]^{-1}\cdot\nabla\tilde{\chi}^2\Big|_{\boldsymbol{a}^{\text{cur}}} \tag{65}$$

The quantity $\boldsymbol{a}^{\text{next}}$ denotes the improved parameter set that converges iteratively to $\boldsymbol{a}^{\text{min}}$. Then, from Eq. 65 an expression is obtained which resembles the iteration sequence of the gradient-descent method [19, 86]:

$$\boldsymbol{a}^{\text{next}} = \boldsymbol{a}^{\text{cur}} + \left[\nabla\nabla\tilde{\chi}^2\Big|_{\boldsymbol{a}^{\text{cur}}}\right]^{-1}\cdot\nabla\tilde{\chi}^2\Big|_{\boldsymbol{a}^{\text{cur}}} \tag{66}$$

The magnitude of $\text{inv}[\nabla\nabla\tilde{\chi}^2(\boldsymbol{a}^{\text{cur}})]$ can be altered adaptively to ensure that $\tilde{\chi}^2(\boldsymbol{a}^{\text{next}}) < \tilde{\chi}^2(\boldsymbol{a}^{\text{cur}})$ [86].

The Levenberg–Marquardt method combines Eqs. 64 and 66 by means of a relative weighting factor, λ, called the Marquardt damping factor [83]. This is done to adapt the relative contribution of the third term in Eq. 63 depending on the proximity between $\boldsymbol{a}^{\text{cur}}$ and $\boldsymbol{a}^{\text{min}}$. Obviously, the Hessian matrix $\nabla\nabla\tilde{\chi}^2(\boldsymbol{a}^{\text{cur}})$ causes imprecision in $d\boldsymbol{a}$ when $\boldsymbol{a}^{\text{cur}}$ is far away from $\boldsymbol{a}^{\text{min}}$. It needs to be damped out so that Eq. 63 renders Eq. 66. Conversely, when $\boldsymbol{a}^{\text{cur}}$ is very close to $\boldsymbol{a}^{\text{min}}$, it is desirable to compute $d\boldsymbol{a}$ using Eq. 64 to benefit from its higher accuracy. In this case the third term in Eq. 63 must be amplified to render Eq. 64. A gradual transition between Eqs. 64 and 66 may be accomplished via

$$\left[\nabla\nabla\tilde{\chi}^2\Big|_{\boldsymbol{a}^{\text{cur}}} - 2\lambda\,\text{diag}\{\nabla\nabla\tilde{\chi}^2\Big|_{\boldsymbol{a}^{\text{cur}}}\}\right]\cdot d\boldsymbol{a} = \nabla\tilde{\chi}^2\Big|_{\boldsymbol{a}^{\text{cur}}} \tag{67}$$

When λ is made so large that the off-diagonal components on the left hand side become negligible compared to the diagonal components, it is seen that Eq. 67 reduces to

$$-2\lambda\,\text{diag}\{\nabla\nabla\tilde{\chi}^2\Big|_{\boldsymbol{a}^{\text{cur}}}\}\cdot d\boldsymbol{a} = \nabla\tilde{\chi}^2\Big|_{\boldsymbol{a}^{\text{cur}}} \tag{68}$$

$$\Longrightarrow \boldsymbol{a}^{\text{next}} = \boldsymbol{a}^{\text{cur}} - \frac{1}{2\lambda}\text{diag}\{\text{inv}[\nabla\nabla\tilde{\chi}^2\Big|_{\boldsymbol{a}^{\text{cur}}}]\}\cdot\nabla\tilde{\chi}^2\Big|_{\boldsymbol{a}^{\text{cur}}} \tag{69}$$

A methodology capable of switching smoothly between Eqs. 64 and 69, via Eq. 67 while varying λ dynamically is given in [19, 83]. Its implementation is given by Algorithm 1 in Appendix C.

Expressions to compute $\nabla\tilde{\chi}^2\big|_{\boldsymbol{a}^{\text{cur}}}$ and $\nabla\nabla\tilde{\chi}^2\big|_{\boldsymbol{a}^{\text{cur}}}$ in Eq. 67 may be derived by differentiating Eq. 60 with respect to the parameters $\boldsymbol{a}$. Differentiating Eq. 60 once yields:

$$\frac{\partial\tilde{\chi}^2}{\partial a_k}\Big|_{\boldsymbol{a}} = -2\sum_{j=1}^{ny-1}\sum_{i=0}^{N-1}\left[\frac{\hat{y}^i_j - y_j(\boldsymbol{a},\boldsymbol{b},\boldsymbol{x}^i,\boldsymbol{y})}{\hat{\sigma}^{i2}_j}\right]\left[\frac{\partial y_j(\boldsymbol{a},\boldsymbol{b},\boldsymbol{x}^i,\boldsymbol{y})}{\partial a_k}\right] \quad 0 \le k < ma \tag{70}$$

and differentiating Eq. 70 once more gives ($0 \le k < ma$, $0 \le l < ma$):

$$\left.\frac{\partial^2 \tilde{\chi}^2}{\partial a_k \partial a_l}\right|_{\boldsymbol{a}} = 2 \sum_{j=1}^{ny-1} \sum_{i=0}^{N-1} \left\{ \frac{1}{\hat{\sigma}_j^{i2}} \left[\frac{\partial y_j(\boldsymbol{a}, \boldsymbol{b}, \boldsymbol{x}^i, \boldsymbol{y})}{\partial a_k} \right] \left[\frac{\partial y_j(\boldsymbol{a}, \boldsymbol{b}, \boldsymbol{x}^i, \boldsymbol{y})}{\partial a_l} \right] - \left[\frac{\hat{y}_j^i - y_j(\boldsymbol{a}, \boldsymbol{b}, \boldsymbol{x}^i, \boldsymbol{y})}{\hat{\sigma}_j^{i2}} \right] \left[\frac{\partial^2 y_j(\boldsymbol{a}, \boldsymbol{b}, \boldsymbol{x}^i, \boldsymbol{y})}{\partial a_k \partial a_l} \right] \right\} \tag{71}$$

For high accuracy applications $\partial^2 \tilde{\chi}^2 / \partial a_k \partial a_l$ may be computed using Eq. 71. But then the computation of $\partial y_j / \partial a_k$ and $\partial^2 y_j / \partial a_k \partial a_l$ requires $ny \times ma + ny \times ma^2$ derivative evaluations which may become burdensome. In the present work $\partial^2 \tilde{\chi}^2 / \partial a_k \partial a_l$ is computed by employing the first term on the right hand side only so that only $ny \times ma$ derivative evaluations are required. Details of how to compute $\nabla \tilde{\chi}^2 \big|_{\boldsymbol{a}^{\text{cur}}}$ and $\nabla\nabla \tilde{\chi}^2 \big|_{\boldsymbol{a}^{\text{cur}}}$ for systems of differential equations are given in Appendix C.

Appendix B: The Runge–Kutta Method and the Rosenbrock Method

For the system of ordinary differential Eq. 54, denoted here by

$$\frac{d\boldsymbol{y}\left(\boldsymbol{a}, \boldsymbol{b}, x, \boldsymbol{y}\right)}{dx} = \boldsymbol{f}\left(\boldsymbol{a}, \boldsymbol{b}, x, \boldsymbol{y}\right), \tag{72}$$

the Runge–Kutta method estimates the solution, $\boldsymbol{y}^{n+1}$, at a next step, $x^{n+1} = x^n + h$, as the sum of the current solution $\boldsymbol{y}^n$ and a linear combination of a set of corrections $\boldsymbol{k}_r^n$ as

$$\boldsymbol{y}^{n+1} = \boldsymbol{y}^n + h \sum_{r=1}^{R} c_r \boldsymbol{k}_r^n. \tag{73}$$

The corrections $\boldsymbol{k}_r^n$ have to be found by solving

$$\boldsymbol{k}_r^n = \boldsymbol{f}\left(\boldsymbol{a}, \boldsymbol{b}, x^n + \alpha_r h, \boldsymbol{y}^n + h \sum_{s=1}^{R} \beta_{rs} \boldsymbol{k}_s^n\right) \tag{74}$$

in $r = 1, \ldots, R$ successive stages. The number of stages, R, the constants α_r and β_{rs}, and, the coefficients c_r determine the accuracy of the method. It is conventional to present α_r, β_{rs}, and c_r in a Butcher-tableau [13, 87–89] as:

$$\begin{array}{c|c} \boldsymbol{\alpha} & \boldsymbol{\beta} \\ \hline & \boldsymbol{c}^T \end{array} = \begin{array}{c|cccc} \boldsymbol{\alpha}_1 & \boldsymbol{\beta}_{11} & \boldsymbol{\beta}_{12} & \boldsymbol{\beta}_{13} \cdots & \boldsymbol{\beta}_{1s} \\ \boldsymbol{\alpha}_2 & \boldsymbol{\beta}_{21} & \boldsymbol{\beta}_{22} & \boldsymbol{\beta}_{23} \cdots & \boldsymbol{\beta}_{2s} \\ \boldsymbol{\alpha}_3 & \boldsymbol{\beta}_{31} & \boldsymbol{\beta}_{32} & \boldsymbol{\beta}_{33} \cdots & \boldsymbol{\beta}_{3s} \\ \cdot & \cdot & \cdot & \cdot \;\cdots & \cdot \\ \cdot & \cdot & \cdot & \cdot \;\cdots & \cdot \\ \boldsymbol{\alpha}_r & \boldsymbol{\beta}_{r1} & \boldsymbol{\beta}_{r2} & \boldsymbol{\beta}_{r3} \cdots & \boldsymbol{\beta}_{rs} \\ \hline & c_1 & c_2 & c_3 \cdots & c_s \end{array} \qquad \begin{array}{l} r = 1, \ldots, R \\ s = 1, \ldots, R \\ \alpha_r = \sum_{s=1}^{R} \beta_{rs} \\ \sum_{r=1}^{R} c_r = 1 \end{array} \tag{75}$$

The fill pattern of β_{rs} determines whether the method is explicit or implicit, and, the extent of implicitness [89, 90]. When $\beta_{rs} = 0$ for $r \le s$, the method is explicit. If $\beta_{rs} = 0$ for $r < s$ and at least one $\beta_{rr} \ne 0$ then the sequence is referred to as a diagonal

Table 2 Butcher-tableaus of the Runge–Kutta and Rosenbrock method. Runge–Kutta method: values of α_r, β_{rs}, $c_r^{5\text{th}}$ (fifth-order accurate) and $c_r^{4\text{th}}$ (fourth-order accurate) are from [91, 92]

Runge–Kutta method. Equations (73) and (76). $\begin{array}{c|c} \boldsymbol{\alpha} & \boldsymbol{\beta} \\ \hline & \boldsymbol{c}^T \end{array} =$

r	s / α_r	1 (β_{rs})	2	3	4	5	6
1	0	0	0	0	0	0	0
2	1/5	1/5	0	0	0	0	0
3	3/10	3/40	9/40	0	0	0	0
4	3/5	3/10	−9/10	6/5	0	0	0
5	1	−11/54	5/2	−70/27	35/27	0	0
6	7/8	1631/55296	175/512	575/13824	44275/110592	253/4096	0
$c_s^{5\text{th}}$		37/378	0	250/621	125/594	0	512/1771
$c_s^{4\text{th}}$		2825/27648	0	18575/48384	13525/55296	277/14336	1/4

Rosenbrock method. Equations (73), (78) and (79). $\begin{array}{c|c|c|c} \boldsymbol{\alpha} & \boldsymbol{\beta}^* & \boldsymbol{\gamma}^* & \boldsymbol{\gamma} \\ \hline & \boldsymbol{c}^T & & \end{array} =$

r	s / α_r	1 (β^*_{rs})	2	3	4	1 (γ^*_{rs})	2	3	4	$\gamma_{rr}=1/2$ / γ_r
1	0	0	0	0	0	0	0	0	0	1/2
2	1	1	0	0	0	−4	0	0	0	−3/2
3	3/5	24/25	3/25	0	0	186/25	6/5	0	0	121/50
4	3/5	24/25	3/25	0	0	−56/125	-27/125	−1/5	0	29/250
$d_s^{4\text{th}}$	19/18	1/4	25/216	125/216						
$d_s^{3\text{rd}}$	98/108	11/72	25/216	0						

Rosenbrock method: values of α_r, β^*_{rs}, γ^*_{rs}, γ_{rr}, γ_r, $d_r^{4\text{th}}$ (fourth-order accurate) and $d_r^{3\text{rd}}$ (third-order accurate) are from [93]

implicit Runge–Kutta method. When $\beta_{rs} = 0$ for $r < s$, all diagonal elements $\beta_{rr} \neq 0$, and identical, then it is termed a singly diagonal implicit Runge–Kutta method. Whenever $\beta_{rs} \neq 0$ if $r > s$ it is called an implicit Runge–Kutta method. This paper employs an explicit Runge–Kutta method as defined by the constants in Table 2 for which the update sequence of successive corrections Eq. 74 simplifies into

$$\boldsymbol{k}_r^n = \boldsymbol{f}\left(\boldsymbol{a}, \boldsymbol{b}, x^n + \alpha_r h, \boldsymbol{y}^n + h\beta_{r1}\boldsymbol{k}_1^n + h\beta_{r2}\boldsymbol{k}_2^n + \ldots + h\beta_{r-1,r-1}\boldsymbol{k}_{r-1}^n\right) \tag{76}$$

whereby each new correction $\boldsymbol{k}_r^n$ is computed from the previous ones, $\{\boldsymbol{k}_1^n, \ldots, \boldsymbol{k}_{r-1}^n\}$.

The Rosenbrock method is a linearised form of the diagonal implicit Runge–Kutta method. The latter has a Butcher-tableau with $\beta_{rs} = 0$ for $r < s$ and at least one $\beta_{rr} \neq 0$ so that the update sequence of the correction factors $\boldsymbol{k}_r^n$ becomes:

$$\boldsymbol{k}_r^n = \boldsymbol{f}\left(\boldsymbol{a}, \boldsymbol{b}, x^n + \alpha_r h, \boldsymbol{y}^n + h\beta_{r1}\boldsymbol{k}_1^n + h\beta_{r2}\boldsymbol{k}_2^n + \ldots + h\beta_{rr}\boldsymbol{k}_r^n\right) \tag{77}$$

The non-zero β_{rr} make it difficult to compute the correction factors because they appear on both sides of Eq. 77. Obtaining $\boldsymbol{k}_r^n$ requires an implicit solution at each stage. To avoid the difficulty and computational burden of having to solve an implicit non-linear algebraic system, it was proposed [12, 13] to linearise the diagonal implicit Runge–Kutta method. By letting

$$\boldsymbol{E} = \boldsymbol{I} - h\gamma_{rr} \left.\frac{\partial \boldsymbol{f}}{\partial \boldsymbol{y}}\right|_{(x^n, \boldsymbol{y}^n)} \quad \text{and} \quad \boldsymbol{f}_x = \left.\frac{\partial \boldsymbol{f}}{\partial x}\right|_{(x^n, \boldsymbol{y}^n)} \tag{78}$$

Eq. 77 can be linearised [13, 93] into ($r = 1, \dots, R; s = 1, \dots, r-1$):

$$\boldsymbol{E} \cdot \boldsymbol{k}_r^n = \boldsymbol{f}\left(x^n + \alpha_r h,\, \boldsymbol{y}^n + h[\beta_{r1}^* \boldsymbol{k}_1^n + \dots + \beta_{rs}^* \boldsymbol{k}_s^n]\right) \\ + (\gamma_{r1}^* \boldsymbol{k}_1^n + \dots + \gamma_{rs}^* \boldsymbol{k}_r^n) + h\gamma_r \boldsymbol{f}_x \tag{79}$$

so that each new correction $\boldsymbol{k}_r^n$ can be obtained from the previous ones, $\{\boldsymbol{k}_1^n, \dots, \boldsymbol{k}_{r-1}^n\}$. The problem independent constants α_r, β_{rs}^*, γ_{rs}^* and γ_r are given in Table 2.

To ensure stability of the integration methods it is necessary to implement adjustable stepsize control while imposing a global relative error tolerance ϵ^{rel} on the increment $y_j^{n+1} - y_j^n$ and absolute error tolerances ϵ_j^{abs} on y_j^{n+1}. This can be accomplished as follows. First, a set of scaling factors η_j^{scal} has to be computed as

$$\eta_j^{\text{scal}} = \max\{\epsilon_j^{\text{abs}}, \epsilon^{\text{rel}} \text{abs}[y_j^{n+1}(h_{\text{try}})]\} \tag{80}$$

where h_{try} denotes an attempted stepsize. Next, the truncation error $\boldsymbol{\epsilon}^{n+1}(h_{\text{try}})$ needs to be computed via

$$\boldsymbol{\epsilon}^{n+1}(h_{\text{try}}) = \begin{cases} h\sum_{r=1}^{6}(c_r^{5\text{th}} - c_r^{4\text{th}})\boldsymbol{k}_r^n & \text{Runge–Kutta} \\ h\sum_{r=1}^{4}(c_r^{4\text{th}} - c_r^{3\text{rd}})\boldsymbol{k}_r^n & \text{Rosenbrock} \end{cases} \tag{81}$$

The scaling factors η_j^{scal} are subsequently used to find the scaled error of the 'worst offender equation', ϵ^{crit}, via:

$$\epsilon^{\text{crit}} = \max\left[\frac{\left|\epsilon_0^{n+1}(h_{\text{try}})\right|}{\eta_0^{\text{scal}}}, \dots, \frac{\left|\epsilon_j^{n+1}(h_{\text{try}})\right|}{\eta_j^{\text{scal}}}, \dots, \frac{\left|\epsilon_{ny-1}^{n+1}(h_{\text{try}})\right|}{\eta_{ny-1}^{\text{scal}}}\right] \tag{82}$$

Once ϵ^{crit} is found, the stepsize can be adjusted by [91]

$$h = \begin{cases} S\,h_{\text{try}}(\epsilon^{\text{crit}})^{-1/p} & \text{if} \quad \epsilon^{\text{crit}} \le 1 \\ S\,h_{\text{try}}(\epsilon^{\text{crit}})^{-1/q} & \text{if} \quad \epsilon^{\text{crit}} > 1 \end{cases} \tag{83}$$

Here, S=0.9 denotes a safety factor. For the Runge–Kutta method $p = 5$ and $q = 4$. For the Rosenbrock method $p = 4$ and $q = 3$. When $\epsilon^{\text{crit}} > 1$, the stepsize is reduced by a $\propto h^q$ scaling. When $\epsilon^{\text{crit}} \le 1$, the stepsize is increased by a $\propto h^p$ scaling.

Appendix C: Combining the Levenberg–Marquardt Method with the Runge–Kutta Method and the Rosenbrock Method

This section describes the combination of the Levenberg–Marquardt method with the Runge–Kutta and the Rosenbrock method. An algorithm for least-squares fitting a system of differential Eq. 56 may be obtained by inspecting Eqs. 60, 67, 70 and 71 to compute $\tilde{\chi}^2(\boldsymbol{a}^{\text{cur}})$, $\nabla\tilde{\chi}^2\big|_{\boldsymbol{a}^{\text{cur}}}$ and $\nabla\nabla\tilde{\chi}^2\big|_{\boldsymbol{a}^{\text{cur}}}$. For a system of algebraic equations, the $y_j(\boldsymbol{a}, \boldsymbol{b}, \boldsymbol{x}^i, \boldsymbol{y})$ needed to compute $\tilde{\chi}^2(\boldsymbol{a}^{\text{cur}})$ by Eq. 60 can be obtained from Eq. 55. The quantities $\partial y_j(\boldsymbol{a}, \boldsymbol{b}, \boldsymbol{x}^i, \boldsymbol{y})/\partial a_k$ needed to compute $\nabla\tilde{\chi}^2\big|_{\boldsymbol{a}^{\text{cur}}}$ and $\nabla\nabla\tilde{\chi}^2\big|_{\boldsymbol{a}^{\text{cur}}}$ via Eqs. 70 and 71 can be obtained by differentiating Eq. 55 with respect to $\boldsymbol{a}$.

To find $y_j(\boldsymbol{a}, \boldsymbol{b}, \boldsymbol{x}^i, \boldsymbol{y})$ and $\partial y_j(\boldsymbol{a}, \boldsymbol{b}, \boldsymbol{x}^i, \boldsymbol{y})/\partial a_k$ for a system of differential Eq. 56 consisting of ny members, it is necessary to formulate an extended system consisting of $ny + ma \times ny$ equations as

$$\frac{d}{dx}\left[y_p\left(\boldsymbol{a}, \boldsymbol{b}, x, \boldsymbol{y}\right)\right] = g_p\left(\boldsymbol{a}, \boldsymbol{b}, x, \boldsymbol{y}\right) \qquad 0 \leq p < ny + ma \times ny \tag{84}$$

where the functions $g_p\left(\boldsymbol{a}, \boldsymbol{b}, x, \boldsymbol{y}\right)$ are related to $f_j\left(\boldsymbol{a}, \boldsymbol{b}, x, \boldsymbol{y}\right)$ in system (56) as

$$g_p\left(\boldsymbol{a}, \boldsymbol{b}, x, \boldsymbol{y}\right) = f_j\left(\boldsymbol{a}, \boldsymbol{b}, x, \boldsymbol{y}\right) \qquad 0 \leq j < ny, \quad p = j \tag{85}$$

$$g_p\left(\boldsymbol{a}, \boldsymbol{b}, x, \boldsymbol{y}\right) = \frac{\partial f_j\left(\boldsymbol{a}, \boldsymbol{b}, x, \boldsymbol{y}\right)}{\partial a_k} \qquad 0 \leq j < ny, \quad 0 \leq k < ma, \tag{86}$$

$$p = ny + ma \times j + k$$

System (84) can be solved numerically by the Runge–Kutta or the Rosenbrock method. Once the solution $\boldsymbol{y}$ has been obtained, the first ny components can be used to compute $\tilde{\chi}^2(\boldsymbol{a}^{\mathrm{cur}})$ by Eq. 60. The components ranging from $ny + 1$ to $ny + ma \times ny$ contain the quantities $\partial y_j(\boldsymbol{a}, \boldsymbol{b}, \boldsymbol{x}^i, \boldsymbol{y})/\partial a_k$ so that $\nabla\tilde{\chi}^2\big|_{\boldsymbol{a}^{\mathrm{cur}}}$ and $\nabla\nabla\tilde{\chi}^2\big|_{\boldsymbol{a}^{\mathrm{cur}}}$ may be computed by Eqs. 70 and 71.

Each equation in system (84) must be provided with an initial condition. With ny differential equations and ma parameters, the members of system (84) indexed by $0 \leq p < ny$ contain the model, and, those by $ny \leq p < ny + ma \times ny$ contain the derivatives with respect $\boldsymbol{a}$. For $0 \leq p < ny$ the initial conditions (x^*, y_p^*) are known from the problem formulation:

$$y_p\left(\boldsymbol{a}, \boldsymbol{b}, x, y_p\right) = y_j^*\left(\boldsymbol{a}, \boldsymbol{b}, x^*, y_j^*\right) \qquad 0 \leq j < ny, \quad p = j \tag{87}$$

However, the initial conditions corresponding to $\partial y_j/\partial a_k$,

$$y_p\left(\boldsymbol{a}, \boldsymbol{b}, x, y_p\right) = \frac{\partial y_j^*\left(a_k, \boldsymbol{b}, x^*, y_j^*\right)}{\partial a_k} \qquad \begin{array}{l} 0 \leq j < ny, \ 0 \leq k < ma \\ p = ny + ma \times j + k \end{array} \tag{88}$$

must be found numerically. This is done by taking the finite difference between the initial conditions $y_j^*(\boldsymbol{a}, \boldsymbol{b}, x^*, y_j^*)$ and a numerically computed perturbed solution at $y_j(\boldsymbol{a} + \Delta\boldsymbol{a}, \boldsymbol{b}, x^*, y_j^*)$ for $0 \leq j < ny$ as:

$$y_p\left(\boldsymbol{a}, \boldsymbol{b}, x, y_p\right) = \frac{\partial y_j^*\left(a_k, \boldsymbol{b}, x^*, y_j^*\right)}{\partial a_k} \approx \frac{y_j(a_k + \Delta a_k, \boldsymbol{b}, x^*, y_j) - y_j^*(a_k, \boldsymbol{b}, x^*, y_j^*)}{\Delta a_k} \tag{89}$$

The perturbed solution is obtained by numerically integrating the original system (72) from x^* to $x_1 = x^* + \Delta x$ and from x^* to $x_2 = x^* + 2\Delta x$, and then by extrapolating the resulting $y_j(a_k + \Delta a_k, \boldsymbol{b}, x_1, y_j)$ and $y_j(a_k + \Delta a_k, \boldsymbol{b}, x_2, y_j)$ as

$$y_j(a_k + \Delta a_k, \boldsymbol{b}, x^*, y_j) = y_j(a_k + \Delta a_k, \boldsymbol{b}, x_1, y_j) \tag{90}$$

$$+ \frac{x^* - x_1}{x_2 - x_1}\left[y_j(a_k + \Delta a_k, \boldsymbol{b}, x_2, y_j) - y_j(a_k + \Delta a_k, \boldsymbol{b}, x_1, y_j)\right] \tag{91}$$

where $0 \leq j < ny$ and $0 \leq k < ma$.

Complications may arise when the initial conditions of the augmented system (84) dependent on the parameter set $\boldsymbol{a}$. To see why, it is helpful to write the Levenberg–

Algorithm 1 Implementation of the Levenberg–Marquardt method in conjunction with the Runge–Kutta method and the Rosenbrock method

A: Prerequisites Define i to index data collection $(\boldsymbol{x}^i, \hat{\boldsymbol{y}}^i_j, \hat{\boldsymbol{\sigma}}^i_j)$. Define `its` ($<$ `maxits`). Define $\tilde{\chi}^2_{\text{crit}}$ (value < 1). Define $\tilde{\chi}^2_0$. Define $\tilde{\chi}^2_{\text{old}}$. *If differential model:* Subdivide $(\boldsymbol{x}^i, \hat{\boldsymbol{y}}^i_j, \hat{\boldsymbol{\sigma}}^i_j)$ into $\{[x_0, x_1], [x_1, x_2], \ldots, [x_i, x_{i+1}]\}$. Define stepsizes h_{min} $(= 10^{-30})$, h_{try}, h_{next}, and h_{init} $(> h_{\text{min}})$. Define `istp` ($<$ `maxstp`).

B: Initialisation Set $i = 0$ and `its` $= 0$. Set $\lambda = 10^{-3}$ [19] in system (67). Provide initial guess in $\boldsymbol{a}^{\text{cur}}$. *If differential model:* Set `istp` $= 0$. Set h_{try} and h_{next} equal to h_{init}. Impose ϵ^{rel} on increment $y^{n+1}_j - y^n_j$, and, ϵ^{abs}_j on y^{n+1}_j.

C: Iteration

C.1: *Differential model*

C.1.1: Set `istp` $= 0$. Set $x^n = x_i$. If ($i = 0 \wedge$ `istp` $= 0$) then set $\boldsymbol{y}^n$ at x^n equal to initial conditions $y_j(\boldsymbol{a}, \boldsymbol{b}, x_0, y_{j0})$. If *Rosenbrock method* then compute Jacobian, $\partial \boldsymbol{f}/\partial \boldsymbol{y}\big|_{(x^n, \boldsymbol{y}^n)}$, and $\partial \boldsymbol{f}/\partial x\big|_{(x^n, \boldsymbol{y}^n)}$ in Eq. 78.

C.1.2: Set $h_{\text{try}} = h_{\text{next}}$. Compare h_{try} with $[x^n, x_{i+1}]$. If $h_{\text{try}} > x_{i+1} - x^n$ then set h_{try} equal to $x_{i+1} - x^n$. If $h_{\text{try}} < h_{\text{min}}$ then spawn error message and exit.

C.1.3: Integrate system (84) to obtain $\boldsymbol{y}$. *Runge–Kutta method.* Compute $\boldsymbol{k}^n_1, \boldsymbol{k}^n_2, \ldots, \boldsymbol{k}^n_r$ using Eq. 76 with h_{try}. *Rosenbrock method.* Update the conditioning matrix $\boldsymbol{E}$ in Eq. 78 and compute $\boldsymbol{k}^n_1, \boldsymbol{k}^n_2, \ldots, \boldsymbol{k}^n_r$ by solving Eq. 79 using h_{try}. Set $x^{n+1} = x^n + h_{\text{try}}$. Compute solution y^{n+1}_j of system (84) at $x^{n+1} = x^n + h_{\text{try}}$ using Eq. 73.

C.1.4: Compute ϵ^{crit} using Eqs. 80–82. Apply ϵ^{crit} to adjust integration stepsize via Eq. 83:

C.1.4.1: If $\epsilon^{\text{crit}} \leq 1$ then set $h_{\text{next}} = Sh_{\text{try}}(\epsilon^{\text{crit}})^{-1/p}$. If $\epsilon^{\text{crit}} > 1$ then set $h_{\text{next}} = Sh_{\text{try}}(\epsilon^{\text{crit}})^{-1/q}$.

C.1.4.2: Increase `istp` by one. If (`istp` $<$ `maxstp`) then return to step C.1.2. If (`istp` $=$ `maxstp`) then spawn error message and exit.

C.1.5: Increase i by one. If $i < nx - 1$ return to C.1.1. If $i = nx - 1$ proceed to C.2.

C.2: Evaluate $\tilde{\chi}^2(\boldsymbol{a}^{\text{cur}})$, $\nabla\tilde{\chi}^2\big|_{\boldsymbol{a}^{\text{cur}}}$ and $\nabla\nabla\tilde{\chi}^2\big|_{\boldsymbol{a}^{\text{cur}}}$ using $\boldsymbol{a}^{\text{cur}}$ and $\left(\boldsymbol{x}^i, \hat{\boldsymbol{y}}^i_j, \hat{\boldsymbol{\sigma}}^i_j\right)$.

C.2.1: If *algebraic model*: evaluate $\{y^i_0, \ldots, y^i_{ny-1}\}$ by Eq. 55. If *differential model*: use $\{y^i_0, \ldots, y^i_{ny-1}\}$ computed by step C.1.

C.2.2: Compute $\tilde{\chi}^2(\boldsymbol{a}^{\text{cur}})$ by Eq. 60, $\nabla\tilde{\chi}^2\big|_{\boldsymbol{a}^{\text{cur}}}$ by Eq. 70, and, $\nabla\nabla\tilde{\chi}^2\big|_{\boldsymbol{a}^{\text{cur}}}$ by Eq. 71.

C.2.3: If `its` $= 0$ then store $\tilde{\chi}^2(\boldsymbol{a}^{\text{cur}})$ in $\tilde{\chi}^2_0$ and $\tilde{\chi}^2_{\text{old}}$.

C.3: If $\tilde{\chi}^2(\boldsymbol{a}^{\text{cur}}) \leq \tilde{\chi}^2_{\text{old}}$:

C.3.1: If $\tilde{\chi}^2(\boldsymbol{a}^{\text{cur}})/\tilde{\chi}^2_0 \leq \tilde{\chi}^2_{\text{crit}}$ then set $\lambda = 0$.

C.3.2: If $\tilde{\chi}^2(\boldsymbol{a}^{\text{cur}})/\tilde{\chi}^2_0 > \tilde{\chi}^2_{\text{crit}}$ then decrease λ by a factor 10.

C.4: If $\tilde{\chi}^2(\boldsymbol{a}^{\text{cur}}) > \tilde{\chi}^2_{\text{old}}$: Increase λ by a factor 10.

C.5: Store $\tilde{\chi}^2(\boldsymbol{a}^{\text{cur}})$ obtained from step C.2.2 into $\tilde{\chi}^2_{\text{old}}$. Solve system (67) to obtain $\boldsymbol{da}$. Update $\boldsymbol{a}^{\text{cur}}$ with $\boldsymbol{da}$ as $\boldsymbol{a}^{\text{cur}} \leftarrow \boldsymbol{a}^{\text{cur}} + \boldsymbol{da}$.

C.6: Increase `its` by one. If `its` $<$ `maxits` return to step C.2.1. If `its` $=$ `maxits` spawn warning that $\tilde{\chi}^2(\boldsymbol{a}^{\text{cur}}) > \tilde{\chi}^2_{\text{old}}$ and $\tilde{\chi}^2(\boldsymbol{a}^{\text{cur}})/\tilde{\chi}^2_0 > \tilde{\chi}^2_{\text{crit}}$.

C.7: Estimate covariance matrix [19] by computing $\text{inv}[\nabla\nabla\tilde{\chi}^2(\boldsymbol{a}^{\text{cur}})]$ in system (67). Return $\boldsymbol{a}^{\text{cur}}$, and, standard errors ϵ_{a_k} as square-root of $\text{diag}[\text{inv}[\nabla\nabla\tilde{\chi}^2(\boldsymbol{a}^{\text{cur}})]]$. Exit.

Marquardt update sequence as $\boldsymbol{a}^* \to \boldsymbol{a}^{(0)} \to \boldsymbol{a}^{(1)} \to \ldots \to \boldsymbol{a}^{(k)} \to \ldots \to \boldsymbol{a}^{\min}$ with $\boldsymbol{a}^*$ denoting the initial guess, $\boldsymbol{a}^{(k)}$ denoting the k-th update, and, $\boldsymbol{a}^{\min}$ the parameter set rendering the optimal model-data match. Prior to each update of $\boldsymbol{a}^{(k)}$, the increment $d\boldsymbol{a}$ is determined by integrating system (84), computing $\nabla\tilde{\chi}^2\big|_{\boldsymbol{a}^{(k)}}$ and $\nabla\nabla\tilde{\chi}^2\big|_{\boldsymbol{a}^k}$, and, solving Eq. 69. When the dependence of the initial conditions on $\boldsymbol{a}^{(k)}$ is not taken into account, this results in a $d\boldsymbol{a}$ which points in a direction other than the projection of the steepest descent of the $\tilde{\chi}^2$ response surface onto the parameter space. Successive updates of $\boldsymbol{a}^{(k)}$ then become so distorted that the algorithm continues indefinitely without getting any closer to $\boldsymbol{a}^{\min}$.

Appendix D: Comparison Between the Classical and Extended Method

Iteration-tableaus of the classical and extended Levenberg–Marquardt method when applied to fit differential Eqs. 24 and 25, and, the analytical solution (26) and (27) to the synthetic data-set in Fig. 1. Prerequisites (Algorithm 1): `maxits` $= 9$, $\tilde{\chi}^2_{\text{crit}} = 10^{-3}$, $\lambda = 10^{-3}$, $h_{\text{init}} = 10^{-5}$, $\epsilon^{\text{rel}} = 10^{-6}$, and $\epsilon_j^{\text{abs}} = 10^{-12}$. Confidence levels from [94].

Confidence levels

For a 99 %, 98 %, 96 %, 95 %, 90 %, 80 %, and 50 % confidence interval multiply the standard errors ϵ_{a_1} and ϵ_{a_2} with the confidence levels: $z_{99\,\%}$=2.58, $z_{98\,\%}$=2.33, $z_{96\,\%}$=2.05, $z_{95\,\%}$=1.96, $z_{90\,\%}$=1.645, $z_{80\,\%}$=1.28, $z_{80\,\%}$=0.6745.

Confidence level, p	99 %	98 %	96 %	95 %	90 %	80 %	50 %
Confidence coefficient, z_p	2.58	2.33	2.05	1.96	1.645	1.28	0.6745
Confidence interval, $a_0 \pm z_p\epsilon_{a_0}$	−0.999	−0.999	−0.999	−0.999	−0.999	−0.999	−0.999
a_0=−0.999; ϵ_{a_0}=0.021	±0.054	±0.049	±0.043	±0.041	±0.035	±0.027	±0.014
Confidence interval, $a_1 \pm z_p\epsilon_{a_1}$	−994.4	−994.4	−994.4	−994.4	−994.4	−994.4	−994.4
a_0=−994.4; ϵ_{a_0}=16.4	±42.3	±38.2	±33.6	±32.1	±26.98	±21.0	±11.1

Classical Levenberg–Marquardt method. Equations (26) and (27).

iter.	λ	a_0	da_0	ϵ_{a_0}	a_1	da_1	ϵ_{a_1}	$\tilde{\chi}^2(\boldsymbol{a})$
init. guess		a_0=−1.2			a_1=−1200			221.682
0	10^{-3}	−0.997	$2.03\cdot10^{-1}$		−988.8	$2.112\cdot10^{2}$		0.49656
1	10^{-4}	−0.999	$-1.82\cdot10^{-3}$		−994.4	$-5.511\cdot10^{0}$		0.37567
2	10^{-5}	−0.999	$-5.73\cdot10^{-7}$		−994.4	$-6.731\cdot10^{-2}$		0.37566
3	10^{-6}	−0.999	$-2.68\cdot10^{-8}$		−994.4	$-6.821\cdot10^{-4}$		0.37566
4	10^{-7}	−0.999	$-2.86\cdot10^{-10}$		−994.4	$-6.891\cdot10^{-6}$		0.37566
final:	0.0	−0.999	$-2.90\cdot10^{-12}$	0.021	−994.4	$-6.961\cdot10^{-8}$	16.4	0.37566

Extended Levenberg–Marquardt method with Runge–Kutta method. Equations (24) and (25). Init. cond. from perturbation (89)–(91).

iter.	λ	a_0	da_0	ϵ_{a_0}	a_1	da_1	ϵ_{a_1}	$\tilde{\chi}^2(\boldsymbol{a})$	integr. steps	deriv. eval.
init. guess		a_0=−1.2			a_1=−1200			221.682	508	3048
0	10^{-3}	−0.997	$2.033\cdot10^{-1}$		−988.8	$2.112\cdot10^{2}$		0.49656	951	5706
1	10^{-4}	−0.998	$-1.816\cdot10^{-3}$		−994.4	$-5.511\cdot10^{0}$		0.37568	880	5280
2	10^{-5}	−0.998	$-5.735\cdot10^{-7}$		−994.4	$-6.730\cdot10^{-2}$		0.37566	869	5214
3	10^{-6}	−0.998	$-2.677\cdot10^{-8}$		−994.4	$-6.821\cdot10^{-4}$		0.37566	869	5214
4	10^{-7}	−0.998	$-2.863\cdot10^{-10}$		−994.4	$-6.892\cdot10^{-6}$		0.37566	877	5262
final:	0.0	−0.998	$-2.911\cdot10^{-12}$	0.021	−994.4	$-6.961\cdot10^{-8}$	16.4	0.37566	861	5166

Extended Levenberg–Marquardt method with Rosenbrock method. Analytical Jacobian. Equations (24) and (25). Init. cond. from perturbation (89)–(91).

iter.	λ	a_0	da_0	ϵ_{a_0}	a_1	da_1	ϵ_{a_1}	$\tilde{\chi}^2(\boldsymbol{a})$	integr. steps	deriv. eval.	Jacbn. eval.
init. guess		a_0=−1.2			a_1=−1200			221.682	506	2024	506
0	10^{-3}	−0.997	$2.033{\cdot}10^{-1}$		−988.8	$2.112{\cdot}10^{2}$		0.49657	1010	4040	1010
1	10^{-4}	−0.998	$-1.816{\cdot}10^{-3}$		−994.4	$-5.511{\cdot}10^{0}$		0.37568	1002	4008	1002
2	10^{-5}	−0.998	$-5.750{\cdot}10^{-7}$		−994.4	$-6.731{\cdot}10^{-2}$		0.37567	995	3980	995
3	10^{-6}	−0.998	$-2.679{\cdot}10^{-8}$		−994.4	$-6.822{\cdot}10^{-4}$		0.37567	1000	4000	1000
4	10^{-7}	−0.998	$-6.115{\cdot}10^{-10}$		−994.4	$-6.900{\cdot}10^{-6}$		0.37567	997	3988	997
final:	0.0	−0.998	$-1.194{\cdot}11^{-11}$	0.021	−994.4	$-6.981{\cdot}10^{-8}$	16.4	0.37567	1000	4000	1000

References

1. Popat, N.R., Catlin, C.A., Arntzen, B.J., Lindstedt, R.P., Hjertager, B.H., Solberg, T., Saeter, O., van den Berg, A.C.: Investigations to improve and assess the accuracy of computational fluid dynamic based explosion models. J. Hazard. Mater. **45**, 1–15 (1996)
2. Watterson, J.K., Connell, I.J., Savill, A.M., Dawes, W.N.: A solution-adaptive mesh procedure for predicting confined explosions. Int. J. Numer. Methods Fluids **26**, 235–247 (1998)
3. Molkov, V.V., Makarov, D., Grigorash, A.: Cellular structure of explosion flames: modeling and large-eddy simulation. Combust. Sci. Technol. **176**, 851–865 (2004)
4. Skjold, T., Arntzen, B., Hansen, O.R., Taraldset, O.J., Storvik, I.E., Eckhoff, R.K.: Simulating dust explosions with the first version of DESC. Trans. Inst. Chem. Eng. B, Process. Saf. Environ. Protect. **83**, 151–160 (2005)
5. Skjold, T., Arntzen, B., Hansen, O.R., Storvik, I.E., Eckhoff, R.K.: Simulation of dust explosions in complex geometries with experimental input from standardized tests. J. Loss Prev. Process Ind. **19**, 210–217 (2006)
6. Eckhoff, R.K.: Current status and expected future trends in dust explosion research. J. Loss Prev. Process Ind. **18**, 225–237 (2005)
7. Sathiah, P., Komen, E., Roekaerts, D.: The role of CFD combustion modeling in hydrogen safety management - I: validation based on small scale experiments. Nucl. Eng. Des. **248**, 93–107 (2012)
8. Sathiah, P., van Haren, S., Komen, E., Roekaerts, D.: The role of CFD combustion modeling in hydrogen safety management - II: validation based on homogeneous hydrogen-air experiments. Nucl. Eng. Des. **252**, 289–302 (2012)
9. Law, C.K.: Propagation, structure, and limit phenomena of laminar flames at elevated pressures. Combust. Sci. Technol. **178**, 335–360 (2006)
10. Kuo, K.K.: Principles of Combustion, 2nd edn. Wiley, New York (2005)
11. Tse, S.D., Zhu, D.L., Law, C.K.: Morphology and burning rates of expanding spherical flames in H_2/O_2/inert mixtures up to 60 atmospheres. In: Proceedings of the Twenty-Eighth Symposium (International) on Combustion, pp. 1793–1800. The Combustion Institute, Pittsburgh (2000)
12. Rosenbrock, H.H.: Some general implicit processes for the numerical solution of differential equations. Comput. J. **5**, 329–330 (1963)
13. Hairer, E., Wanner, G.: Solving Ordinary Differential Equations, 2nd edn. II. Stiff and Differential-Algebraic Problems. Springer Series in Computational Mathematics, vol. 14. Springer, Berlin (1996).
14. Van den Bulck, E.: Closed algebraic expressions for the adiabatic limit value of the explosion constant in closed volume combustion. J. Loss Prev. Process Ind. **18**, 35–42 (2005)
15. Tennekes, H., Lumley, J.L.: A First Course in Turbulence. MIT Press, Cambridge, MA (1972)
16. Hinze, J.O.: Turbulence, 2nd edn. McGraw-Hill Series in Mechanical Engineering, New York (1975)
17. Pope, S.B.: Turbulent Flows. Cambridge University Press, Cambridge, UK (2000)
18. Yakhot, V.: Propagation velocity of premixed turbulent flames. Combust. Sci. Technol. **60**, 191–214 (1988)
19. Press, W.H., Teukolsky, S.A., Vetterling, W.T., Flannery, B.P.: Numerical Recipes, The Art of Scientific Computing, 3rd edn. Cambridge University Press, Cambridge, UK (2007)

20. Knuth, D.E.: The Art of Computer Programming, Seminumerical Algorithms, vol. 2, 3rd edn. Addison-Wesley, Reading, MA (1997)
21. Box, G.E.P., Muller, M.E.: A note on the generation of random normal deviates. Ann. Math. Stat. **29**, 610–611 (1958)
22. Muller, M.E.: A comparison of methods for generating normal deviates on digital computers. J. ACM **6**(3), 376–383 (1959)
23. Press, W.H., Teukolsky, S.A., Vetterling, W.T., Flannery, B.P.: Numerical Recipes in C++, The Art of Scientific Computing, 2nd edn. Cambridge University Press, Cambridge, UK (2002)
24. Enright, W.H., Pryce, J.D.: Two FORTRAN packages for assessing initial value problems. ACM Trans. Math. Softw. **13**, 1–27 (1987)
25. Gear, C.W.: The automatic integration of stiff ordinary differential equations. Inf. Process. **68**, 187–193 (1969)
26. Lapidus, L., Aiken, R.C., Liu, Y.A.: The occurrence and numerical solution of physical and chemical systems having widely varying time constants. In: Willoughby, R.A. (ed.) Stiff Differential Systems, pp. 187–200. Plenum, New York (1974)
27. Luss, D., Amundson, N.R.: Stability of batch catalytic fluidized beds. AIChE J., Part A **14**, 211–221 (1968)
28. Dahoe, A.E., Zevenbergen, J.F., Lemkowitz, S.M., Scarlett, B.: Dust explosions in spherical vessels: the role of flame thickness in the validity of the 'cube-root-law'. J. Loss Prev. Process Ind. **9**(1), 33–44 (1996)
29. Dahoe, A.E., de Goey, L.P.H.: On the determination of the laminar burning velocity of closed vessel explosions. J. Loss Prev. Process Ind. **16**, 457–478 (2003)
30. Dahoe, A.E.: Laminar burning velocities of hydrogen-air mixtures from closed vessel gas explosions. J. Loss Prev. Process Ind. **18**, 152–166 (2005)
31. Dahoe, A.E., Cant, R.S., Scarlett, B.: On the decay of turbulence in the 20-liter explosion sphere. Flow Turbul. Combust. **67**, 159–184 (2001)
32. Dahoe, A.E., van der Nat, K., Braithwaite, M., Scarlett, B.: On the effect of turbulence on the maximum explosion pressure of a dust deflagration. KONA – Powder Part. **19**, 178–196 (2001)
33. Dahoe, A.E.: Dust explosions: a study of flame propagation. Ph.D. thesis, Delft University of Technology, Delft, The Netherlands (2000)
34. Bradley, D., Lau, A.K.C., Lawes, M.: Flame stretch as a determinant of turbulent burning velocity. Philos. Trans. R. Soc. Lond. Ser. A: Math. Phys. Sci. **338**, 359–387 (1992)
35. Miller, J.A., Mitchell, R.E., Smooke, M.D., Kee, R.J.: Toward a comprehensive chemical kinetic mechanism for the oxidation of acetylene: comparison of model predictions with results from flame and shock tube experiments. In: Proceedings of the Nineteenth Symposium (International) on Combustion, pp. 181–196. The Combustion Institute, Pittsburgh (1982)
36. Andrews, G.E., Bradley, D., Lwakabamba, S.B.: Turbulence and turbulent flame propagation – a critical appraisal. Combust. Flame **24**, 285–304 (1975)
37. Gülder, Ö.L.: Turbulent premixed flame propagation models for different combustion regimes. In: Proceedings of the Twenty-Third Symposium (International) on Combustion, pp. 743–750. The Combustion Institute, Pittsburgh (1990)
38. Lipatnikov, A.N., Chomiak, J.: Turbulent flame speed and thickness: phenomenology, evaluation, and application in multi-dimensional simulations. Prog. Energy Combust. Sci. **28**, 1–74 (2002)
39. Dixon-Lewis, G., Wilson, J.G.: A method for the measurement of the temperature distribution in the inner cone of a Bunsen flame. Trans. Faraday Soc. **46**, 1106–1114 (1951)
40. Janisch, G.: Geschwindigkeits- und Temperaturverteilung in einer ebenen laminaren Flammenfront. Chem. Ing. Tech. **43**, 561–565 (1971)
41. Andrews, G.E., Bradley, D.: The burning velocity of methane-air mixtures. Combust. Flame **19**, 275–288 (1972)
42. Damköhler, G.: Der einfluss der Turbulenz auf die Flammengeschwindigkeit in Gasgemischen. Z. Elektrochem. **46**, 601–626 (1940)
43. Damköhler, G.: The effect of turbulence on the flame velocity in gas mixtures. Technical Memorandum NACA TM 1112. National Advisory Committee for Aeronautics, Washington (1947)
44. Schelkin, K.I.: On combustion in a turbulent flow. Sov. Phys. – Tech. Phys. **13**, 520–530 (1943)
45. Schelkin, K.I.: On combustion in a turbulent flow. NACA Technical Memorandum 1110. National Advisory Committee for Aeronautics, Washington (1947). Original: J. Tech. Phys. (USSR) **13**(9–10), 520–530 (1943)
46. Karlovitz, B., Denniston, D.W., Wells, F.E.: Investigation of turbulent flames. J. Chem. Phys. **19**(5), 541–547 (1951)

47. Taylor, G.I.: Diffusion by continuous movements. Proc. Lond. Math. Soc. **20**, 196–212 (1922)
48. Leason, D.B.: Turbulence and flame propagation in premixed gases. Fuel **30**, 233–239 (1951)
49. Tucker, M.: Interaction of a free flame front with a turbulence field. Technical Note NACA TN 3407. National Advisory Committee for Aeronautics, Washington (1955)
50. Clavin, P., Williams, F.A.: Theory of premixed-flame propagation in large-scale turbulence. J. Fluid Mech. **90**, 589–604 (1979)
51. Clavin, P., Williams, F.A.: Effects of molecular diffusion and of thermal expansion on the structure and dynamics of premixed flames in turbulent flows of large scale and low turbulence. J. Fluid Mech. **116**, 251–282 (1982)
52. Klimov, A.M.: Premixed turbulent flames – interplay of hydrodynamic and chemical phenomena. Prog. Astronaut. Aeronaut. **88**, 133–146 (1983)
53. Abdel-Gayed, R.G., Ali-Khishali, K.J., Bradley, D.: Turbulent burning velocity and flame straining in explosions. Philos. Trans. R. Soc. Lond. Ser. A: Math. Phys. Sci. **391**, 393–414 (1984)
54. Pope, S.B., Anand, M.S.: Flamelet and distributed combustion in premixed turbulent flames. In: Proceedings of the Twentieth Symposium (International) on Combustion, pp. 403–410. The Combustion Institute, Pittsburgh (1984)
55. Kerstein, A.R.: Pair-exchange model of turbulent premixed flame propagation. In: Proceedings of the Twenty-First Symposium (International) on Combustion, pp. 1281–1289. The Combustion Institute, Pittsburgh (1986)
56. Gouldin, F.C.: An application of fractals to modeling premixed turbulent flames. Combust. Flame **68**, 249–266 (1987)
57. Lovejoy, S.: The area-perimeter relation for rain and cloud areas. Science **216**, 185–187 (1982)
58. Hentschel, H.G.E., Procaccia, I.: Relative diffusion in turbulent media: the fractal dimension of clouds. Phys. Rev. A **29**, 1461–1470 (1984)
59. Sreenivasan, K.R., Meneveau, C.: The fractal facets of turbulence. J. Fluid Mech. **173**, 357–186 (1986)
60. Abdel-Gayed, R.G., Bradley, D.: Derivation of turbulent transport coefficients from turbulent parameters in isotropic turbulence. Trans. ASME J. Fluids Eng. **99**, 732–736 (1977)
61. Peters, N.: Laminar flamelet concepts in turbulent combustion. In: Proceedings of the Twenty-First Symposium (International) on Combustion, pp. 1231–1250. The Combustion Institute, Pittsburgh (1988)
62. Peters, N.: Length scales in laminar and turbulent flames. Prog. Astronaut. Aeronaut. **135**, 155–182 (1991)
63. Kerstein, A.R.: Simple derivation of Yakhot's turbulent premixed flamespeed formula. Combust. Sci. Technol. **60**, 163–165 (1988)
64. Poinsot, T., Veynante, D.: Theoretical and Numerical Combustion, 2nd edn. Edwards, Philadelphia (2005)
65. Kerstein, A.R., Ashurst, W., Williams, F.A.: Field equation for interface propagation in an unsteady homogeneous flow field. Phys. Rev. A **37**, 2728–2731 (1988)
66. Liu, Y., Lenze, B.: The influence of turbulence on the burning velocity of premixed CH4–H2 flames with different laminar burning velocities. In: Proceedings of the Twenty-Second Symposium (International) on Combustion, pp. 747–754. The Combustion Institute, Pittsburgh (1988)
67. Leuckel, W., Nastoll, W., Zarzalis, N.: Experimental investigation of the influence of turbulence on the transient premixed flame propagation inside closed vessels. In: Proceedings of the Twenty-Third Symposium (International) on Combustion, pp. 729–734. The Combustion Institute, Pittsburgh (1990)
68. Abdel-Gayed, R.G., Bradley, D., Lawes, M.: Turbulent burning velocities: a general correlation in terms of straining rates. Philos. Trans. R. Soc. Lond. Ser. A: Math. Phys. Sci. **414**, 389–413 (1987)
69. Zimont, V.L., Lipatnikov, A.N.: A numerical model of premixed turbulent combustion of gases. Chem. Phys. Rep. **14**, 993–1025 (1995)
70. Bray, K.N.C., Libby, P.A., Moss, J.B.: Flamelet crossing frequencies and mean reaction rates in premixed turbulent combustion. Combust. Sci. Technol. **41**, 143–172 (1984)
71. Bray, K.N.C., Libby, P.A., Moss, J.B.: Unified modelling approach for premixed turbulent combustion – part I: general formulation. Combust. Flame **61**, 87–102 (1985)
72. Bray, K.N.C., Libby, P.A.: Passage times and flamelet crossing frequencies in premixed turbulent combustion. Combust. Sci. Technol. **47**, 253 (1986)
73. Shy, S.S., Lin, W.J., Wei, J.C.: An experimental correlation of turbulent burning velocities for premixed turbulent methane-air combustion. Philos. Trans. R. Soc. Lond. Ser. A: Math. Phys. Sci. **456**, 1997–2019 (2000)

74. Hamberger, P., Schneider, H., Jamois, D., Proust, C.: Correlation of turbulent burning velocity and turbulence intensity for starch dust air mixtures. In: Proceedings of the Third European Combustion Meeting, 11–13 April 2007, Chania, Greece (2007)
75. Bray, K.N.C.: Studies of the turbulent burning velocity. Philos. Trans. R. Soc. Lond. Ser. A: Math. Phys. Sci. **431**, 315–335 (1990)
76. Schneider, H., Proust, C.: Determination of turbulent burning velocities of dust air mixtures with the open tube method. J. Loss Prev. Process Ind. **20**, 470–476 (2007)
77. Dahoe, A.E., van Velzen T.J., Sluijs, L.P., Neervoort, F.J., Leschonski, S., Lemkowitz, S.M., van der Wel, P.G.J., Scarlett, B.: Construction and operation of a 20-litre dust explosion sphere at and above atmospheric conditions. In: Mewis, J.J., Pasman, H.J., De Rademaeker, E.E. (eds.) Loss Prevention and Safety Promotion in the Process Industries, Proceedings of the 8th International Symposium, vol. 2, pp. 285–302. European Federation of Chemical Engineering (EFCE), Elsevier Science (1995)
78. Dahoe, A.E., van der Wel, P.G.J., Lemkowitz, S.M., Leschonski, S., Scarlett, B.: Effects of turbulence on dust explosions at elevated initial pressures. In: Leschonski, K. (ed.) PARTEC 95, 6th European Symposium Particle Characterization, pp. 257–266. European Federation of Chemical Engineering (EFCE), Nürnberg Messe GmbH (1995)
79. Dahoe, A.E., Zevenbergen, J.F., Lemkowitz, S.M., Scarlett, B.: Dust explosion testing with the strengthened 20-litre sphere. In: The Seventh International Colloquium on Dust Explosions, pp. 7.30–7.46. Christian Michelsen Research AS (1996)
80. Siwek, R.: 20-l laborapparatur für die Bestimmung der explosionskenngrößen brennbarer Stäube. Ph.D. thesis, Technical University of Winterthur, Winterthur, Switzerland (1977)
81. Borghi, R.: On the structure and morphology of turbulent premixed flames. In: Casci, C. (ed.) Recent Advances in the Aerospace Sciences, pp. 117–138. Plenum Publishing Corporation (1985)
82. Goodwin, D.G.: Cantera C++ User's Guide. California Institute of Technology (2002)
83. Marquardt, D.W.: An algorithm for least-squares estimation of nonlinear parameters. SIAM J. Appl. Math. **11**, 431–441 (1963)
84. Williams, F.A.: Combustion Theory: The Fundamental Theory of Chemically Reacting Flow Systems. Combustion Science and Engineering Series, 2nd edn. The Benjamin/Cummings Publishing Company, Menlo Park, California (1985)
85. Lawson, C.L., Hanson, R.J.: Solving Least Squares Problems. SIAM Classics in Applied Mathematics, vol. 15. Society for Industrial and Applied Mathematics, Philadelphia (1995)
86. Dennis, J.E., Schnabel, R.B.: Numerical Methods for Unconstrained Optimization and Nonlinear Equations. SIAM Classics in Applied Mathematics, vol. 16. Society for Industrial and Applied Mathematics, Philadelphia (1996)
87. Butcher, J.C.: Numerical Methods for Ordinary Differential Equations. Wiley, Chichester, England (2003)
88. Lambert, J.D.: Numerical methods for ordinary differential systems: the initial value problem. Wiley, Chichester (1991)
89. Hairer, E., Norsett, S.P., Wanner, G.: Solving ordinary differential equations. I. Nonstiff problems. In: Springer Series in Computational Mathematics, vol. 8, 2nd edn. Springer, Berlin (1993)
90. Butcher, J.C.: Implicit Runge–Kutta processes. Math. Comput. **18**, 50–64 (1964)
91. Press, W.H., Teukolsky, S.A., Vetterling, W.T., Flannery, B.P.: Numerical Recipes in C, The Art of Scientific Computing, 2nd edn. Cambridge University Press, Cambridge, UK (1992)
92. Cash, J.R., Karp, A.H.: A variable order Runge–Kutta method for initial value problems with rapidly varying right-hand sides. ACM Trans. Math. Softw. **16**, 201–222 (1990)
93. Shampine, L.F.: Implementation of Rosenbrock methods. ACM Trans. Math. Softw. **8**, 93–113 (1982)
94. Spiegel, M.R., Stephens, L.J.: Theory and Problems of Statistics. Schaum's Outline Series, 3rd edn. McGraw-Hill, New York (1999)